

Allosteric activation or inhibition of PI3Ky mediated through conformational changes in the p110 γ helical domain

Reviewed Preprint

Published from the original preprint after peer review and assessment by eLife.

[About eLife's process](#)

Reviewed preprint version 2

June 12, 2023

Reviewed preprint version 1



May 23, 2023 (this version)

Posted to preprint server

April 12, 2023

Sent for peer review

April 12, 2023

Noah J Harris, Meredith L Jenkins, Sung-Eun Nam, Manoj K Rathinaswamy, Matthew AH Parson, Harish Ranga-Prasad, Udit Dalwadi, Brandon E Moeller, Eleanor Sheekey, Scott D Hansen, Calvin K Yip , John E Burke 

Department of Biochemistry and Microbiology, University of Victoria, Victoria, British Columbia, V8W 2Y2, Canada •

Department of Biochemistry and Molecular Biology, The University of British Columbia, Vancouver, British

Columbia V6T 1Z3, Canada • Department of Chemistry and Biochemistry, Institute of Molecular Biology, University

of Oregon, Eugene, OR 97403

 https://en.wikipedia.org/wiki/Open_access

 Copyright information

Abstract

PI3Ky is a critical immune signaling enzyme activated downstream of diverse cell surface molecules, including Ras, PKC β activated by the IgE receptor, and G $\beta\gamma$ subunits released from activated GPCRs. PI3Ky can form two distinct complexes, with the p110 γ catalytic subunit binding to either a p101 or p84 regulatory subunit, with these complexes being differentially activated by upstream stimuli. Here using a combination of Cryo electron microscopy, HDX-MS, and biochemical assays we have identified novel roles of the helical domain of p110 γ in regulating lipid kinase activity of distinct PI3Ky complexes. We defined the molecular basis for how an allosteric inhibitory nanobody potently inhibits kinase activity through rigidifying the helical domain and regulatory motif of the kinase domain. The nanobody did not block either p110 γ membrane recruitment or Ras/G $\beta\gamma$ binding, but instead decreased ATP turnover. We also identified that p110 γ can be activated by dual PKC β helical domain phosphorylation leading to partial unfolding of an N-terminal region of the helical domain. PKC β phosphorylation is selective for p110 γ -p84 compared to p110 γ -p101, driven by differential dynamics of the helical domain of these different complexes. Nanobody binding prevented PKC β mediated phosphorylation. Overall, this work shows an unexpected allosteric regulatory role of the helical domain of p110 γ that is distinct between p110 γ -p84 and p110 γ -p101, and reveals how this can be modulated by either phosphorylation or allosteric inhibitory binding partners. This opens possibilities of future allosteric inhibitor development for therapeutic intervention.

eLife assessment

This study presents **fundamental** new insight into the regulatory apparatus of PI3Kgamma, a crucial kinase in signaling pathways that control the immune response and cancer. A suite of biophysical and biochemical approaches provide **convincing** evidence for new sites of allosteric control over enzyme activity. The rigorous findings provide structure and dynamic information that may be exploited in efforts to control PI3Kgamma activity in a therapeutic setting.

Introduction

The class I phosphoinositide 3 kinases (PI3Ks) are master regulators of myriad functions through their generation of the lipid signalling molecule phosphatidylinositol 3,4,5-trisphosphate (PIP₃) downstream of cell surface receptors (Burke and Williams, 2015 [↗](#); Rathinaswamy and Burke, 2019 [↗](#); Vanhaesebroeck et al., 2021 [↗](#); Vasan and Cantley, 2022 [↗](#)). The class I PI3Ks can be further subdivided into the class IA and class IB subfamilies, with class IB PI3Ks being critical in immune signalling, and are composed of a single p110γ catalytic subunit that can bind to either a p101 or p84 regulatory subunit (Hawkins and Stephens, 2015 [↗](#); Lanahan et al., 2022 [↗](#); Okkenhaug, 2013 [↗](#)). The two PI3Kγ complexes (either p110γ-p84 or p110γ-p101) play essential and independent roles in both the adaptative and innate immune systems. PI3Kγ has shown promise as a therapeutic target, primarily as an immunomodulator of the tumor microenvironment leading to enhanced anti-tumor immune responses (De Henau et al., 2016 [↗](#); Kaneda et al., 2016b [↗](#)). Multiple isoform selective small molecule ATP competitive inhibitors of p110γ are in clinical trials for multiple forms of human cancers (Li et al., 2021 [↗](#)). However, all inhibitors currently developed towards p110γ act as ATP competitive inhibitors, showing equal potency against both p110γ-p84 or p110γ-p101 complexes.

Detailed experiments on the role of p110γ in mice show that knockout of both p101 and p84 leads to PIP₃ levels that are equivalent to knockout of p110γ, showing that all cellular PI3Kγ activity requires the presence of either a p84 or p101 regulatory subunit (Rynkiewicz et al., 2020 [↗](#)). The two complexes are differentially activated by membrane localised receptors, including G-protein coupled receptors (Li et al., 2000 [↗](#); Stephens et al., 1997 [↗](#)), Ras (Jin et al., 2020 [↗](#); Kurig et al., 2009 [↗](#)), toll like receptors (TLRs) (Luo et al., 2018 [↗](#)), and the IgE antigen receptor (Laffargue et al., 2002 [↗](#); Walser et al., 2013 [↗](#)). This leads to the different complexes driving unique immune responses, with p110γ-p101 involved in chemotaxis in neutrophils (Bohnacker et al., 2009 [↗](#); Deladeriere et al., 2015 [↗](#)), and p110γ-p84 involved in reactive oxide production. Differential activation of unique PI3Kγ complexes downstream of GPCRs and Ras is caused by the ability of p101 to directly bind to Gβγ subunits downstream of activated GPCRs, with this being lost in p84, making p110γ-p84 activation by Gβγ dependent on Ras mediated membrane recruitment (Rathinaswamy et al., 2023 [↗](#); Kurig et al., 2009 [↗](#); Rynkiewicz et al., 2020 [↗](#)). Activation of PI3Kγ downstream of the IgE antigen receptor is driven by calcium mediated activation of protein kinase Cβ, leading to the selective phosphorylation and activation of p110γ at S582 (Walser et al., 2013 [↗](#)), with this putatively only occurring in p110γ-p84 and not p110γ-p101. The full molecular mechanisms underlying how phosphorylation of p110γ is selective for different p84 or p101 complexes, and how it activates lipid kinase activity are poorly understood.

Extensive biophysical approaches including cryo electron microscopy (cryo-EM), X-ray crystallography, and hydrogen deuterium exchange mass spectrometry (HDX-MS) have provided extensive insight into the molecular underpinnings of how p110γ associates with both p101 and p84, how they are differentially activated by Ras and GPCR signals, and how they can be activated

on lipid membranes (Pacold et al., 2000 [↗](#); Walker et al., 1999 [↗](#); Rathinaswamy et al., 2021c [↗](#), 2021a [↗](#); Gangadhara et al., 2019 [↗](#); Vadas et al., 2013 [↗](#); Rathinaswamy et al., 2023 [↗](#)). The p110 γ catalytic subunit is composed of an adaptor binding domain (ABD), a Ras binding domain (RBD), a C2 domain, a helical domain, and a bi-lobal kinase domain (Rathinaswamy et al., 2021a [↗](#); Walker et al., 1999 [↗](#)). A set of helices positioned C-terminal to the activation loop in the kinase domain play a critical role in regulating activity, with this region referred to as the regulatory motif (Rathinaswamy et al., 2021c [↗](#)). The p110 γ isoform is unique in that it is inhibited in the absence of a regulatory subunit, with this driven by an autoinhibitory conformation of the regulatory motif, that is proposed to require membrane association to disrupt (Gangadhara et al., 2019 [↗](#)). The regulatory motif is a common site of activating mutations in the other class I PI3K isoforms (Jenkins et al., 2023 [↗](#)), with p110 γ having rare activating oncogenic mutants in this region (Rathinaswamy et al., 2021c [↗](#)). The p110 γ subunit interacts with both p84 and p101 at an interface composed of the C2 domain, and the linkers between the RBD-C2 and C2-helical domains (Rathinaswamy et al., 2023 [↗](#), 2021a [↗](#)). The p110 γ -p84 complex forms a more dynamic complex compared to p110 γ -p101 (Rathinaswamy et al., 2023 [↗](#); Shymanets et al., 2013 [↗](#)), however, no clear unique regulatory role of this difference in dynamics has been identified.

The fundamental roles of p110 γ in inflammatory processes has made it a therapeutic target in many pathological conditions, including asthma (Campa et al., 2018 [↗](#)), arthritis (Camps et al., 2005 [↗](#)), obesity (Becattini et al., 2011 [↗](#); Breasson et al., 2017 [↗](#)), and cancer (De Henau et al., 2016 [↗](#); Kaneda et al., 2016a [↗](#), 2016b [↗](#)). There are significant side effects from non-isoform selective PI3K inhibitors (Bohnacker et al., 2017 [↗](#); Vanhaesebroeck et al., 2021 [↗](#)), which has driven the development of highly p110 γ selective small molecule inhibitors (Bell et al., 2012 [↗](#); Evans et al., 2016 [↗](#); Gangadhara et al., 2019 [↗](#)). However, all p110 γ inhibitors will target both p110 γ -p101 and p110 γ -p84, so there is a potential for the development of allosteric inhibitors outside of the ATP binding site. Initial promise has been reported for the development of class IA p110 α oncogene specific allosteric inhibitors. However, further investigation of the molecular mechanisms underlying p110 γ regulation will be required for the discovery of regions that can be targeted for allosteric inhibitor development.

Here we report critical roles of the helical domain of p110 γ in both activation and inhibition of lipid kinase activity. We characterised an allosteric inhibitory nanobody (NB7) that potently inhibits p110 γ activity. Cryo-EM was used to define the inhibitory interface, which is composed of the helical domain, the ABD-RBD linker, and the regulatory motif of the kinase domain of p110 γ . The region that the nanobody binds to is in close spatial proximity to a previously identified PKC β phosphorylation site (S582) in the helical domain, and oncogenic activating mutants in the regulatory motif. We fully characterised the activity and dynamics of stoichiometrically PKC β phosphorylated p110 γ , leading to the discovery of a novel additional phosphorylation site (S594/S595). PKC β phosphorylation was highly selective for p110 γ and p110 γ -p84, with limited phosphorylation of p110 γ -p101. Hydrogen deuterium exchange mass spectrometry (HDX-MS) analysis showed that phosphorylation of p110 γ leads to unfolding of the N-terminal region of the helical domain, and increased kinase activity. The presence of the inhibitory nanobody significantly blocks PKC β phosphorylation, with phosphorylated p110 γ showing no detectable binding to NB7. Overall, this work provides unique insight into the critical role of the helical domain in controlling p110 γ activity, and how phosphorylation and binding partners can modify this regulation. It also reveals a unique binding site located at the interface of the helical and kinase domain that can be targeted for future allosteric inhibitor design.

Results

Molecular mechanism of nanobody inhibition of p110 γ

We previously identified multiple nanobodies that inhibited the activity of p110 γ . One from this group (denoted NB7 throughout the manuscript) potently inhibited the membrane mediated activation of p110 γ -p84 by both Ras and G $\beta\gamma$, with HDX-MS experiments mapping the NB7 binding interface to the RBD, helical and kinase domains (Rathinaswamy et al., 2021b [↗](#)). We originally hypothesized that NB7 worked by sterically inhibiting Ras binding to the RBD domain of p110 γ . To further explore the molecular mechanism of inhibition we purified all complexes of p110 γ (p110 γ apo, p110 γ -p84, p110 γ -p101) along with the NB7 nanobody. The SDS-PAGE of all proteins utilised in this study are shown in the source data file included in the supplemental information.

To define the mechanism concerning how NB7 inhibits PI3K activity we analyzed how this nanobody inhibited all class IB PI3K complexes (p110 γ , p110 γ -p84, p110 γ -p101) upon activation by lipidated G $\beta\gamma$ subunits. Intriguingly, we found that all three forms of p110 γ were potently inhibited by NB7 (**Fig. 1A** [↗](#)). While the IC₅₀ measured for the three complexes was different, this is likely mainly due to the dramatic difference in protein required to measure lipid kinase activity *in vitro* (~300 nM for p110 γ apo/p110 γ -p84, and ~10 nM for p110 γ -p101, respectively). This suggested that the mechanism of inhibition was not driven by a steric block of Ras association through the RBD, as previously proposed (Rathinaswamy et al., 2021b [↗](#)). We examined the binding of this nanobody to all complexes using biolayer interferometry (BLI). The nanobody bound equivalently tightly to all complexes, with ~2 nM potency for p110 γ , p110 γ -p84, and p110 γ -p101 (**Fig. 1B** [↗](#)). We also tested binding of the nanobody to all class IA PI3Ks, and there was no detectable binding to p110 α , p110 β , and p110 δ (**Fig. 1C** [↗](#)).

To further understand the mechanism by which this nanobody blocked lipid kinase activity we measured the bulk membrane recruitment dynamics of fluorescently labeled Dy647-p84-p110 γ on supported lipid bilayers (SLBs) using Total Internal Reflection Fluorescence (TIRF) Microscopy. We found that the nanobody had no effect on membrane recruitment of p110 γ -p84 on bilayers containing membrane-tethered Ras(GTP) and G $\beta\gamma$ (**Fig. 1D-F** [↗](#)). Membrane binding was not affected when the nanobody was spiked into samples containing membrane associated Dy647-p84-p110 γ (**Fig. 1D** [↗](#)). Similarly, pre-incubation of Dy647-p84-p110 γ with 500 nM NB7 did not perturb membrane association of the kinase when flowed over a supported membrane (**Fig. 1E** [↗](#)).

We wanted to define the molecular mechanism of how nanobody NB7 was a potent allosteric inhibitor of lipid kinase activity. We purified the complex of nanobody NB7 bound to p110 γ -p84 to homogeneity by gel filtration. Using this sample, we obtained a cryo-EM reconstruction of the complex of nanobody (NB7)-bound p110 γ at 3.0-Å overall resolution from 149,603 particles (**Figs. 2A-D** [↗](#), **S1** [↗](#) and **supplemental table 1** [↗](#)). The density map was of sufficient quality to perform automated and manual construction of the p110 γ -NB7 complex, with unambiguous building of the interfacial contacts between NB7 and p110 γ . Nanobody binding did not induce any large-scale conformational changes of p110 γ , as the structure of p110 γ bound to NB7 was similar to the apo p110 γ crystal structure or p110 γ -p101 cryo-EM structure (Fig. S2). The lowest local resolution was in the ABD domain, with increased B-factors of the ABD in the p110 γ -NB7 structure compared to p110 γ -p101 (Fig. S2). This is consistent with the concept that ABD flexibility plays an important role in class I PI3K regulation (Liu et al., 2022 [↗](#)).

The interface between NB7 and p110 γ was extensive, with ~1200 Å² of buried surface area, with interactions of the ABD-RBD linker, N-terminus of the helical domain, and the regulatory motif at the turn between α 8- α 9 (1022-1026aa). This location in the regulatory motif is where both activating oncogenic (R1021C) and inhibitory loss of function mutants have been identified (R1021P) (Takeda et al., 2019 [↗](#)), as well as a putative inhibitory phosphorylation site (T1024) (Perino et al., 2011 [↗](#)). The resolution was sufficient to unambiguously build the three

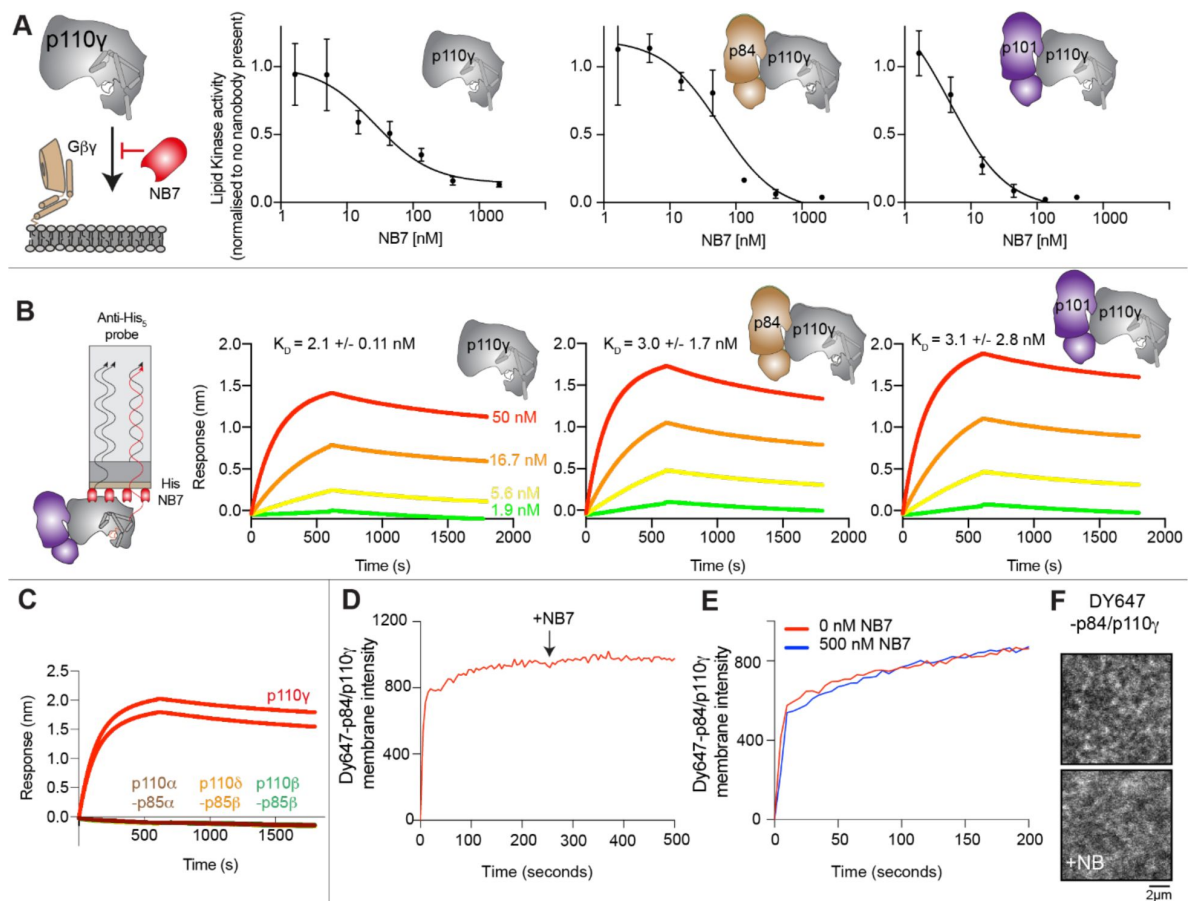


Figure 1.

The inhibitory nanobody NB7 binds tightly to all p110γ complexes and inhibits kinase activity, but does not prevent membrane binding

A. Cartoon schematic depicting nanobody inhibition of activation by lipidated Gβγ (1.5 μM final concentration). Lipid kinase assays show a potent inhibition of lipid kinase activity with increasing concentrations of NB7 (3-3000 nM) for the different complexes. The protein concentration of p110γ (300 nM), p110γ-p84 (330 nM) and p110γ-p101 (12 nM) was different due to intrinsic differences of each complex to be activated by lipidated Gβγ.

B. Association and dissociation curves for the dose response of His-NB7 binding to p110γ, p110γ-p84 and p110γ-p101 (50 – 1.9 nM) is shown. A cartoon schematic of BLI analysis of the binding of immobilized His-NB7 to p110γ is shown on the left. Dissociation constants (K_D) were calculated based on a global fit to a 1:1 model for the top three concentrations and averaged with error shown.

C. Association and dissociation curves for His-NB7 binding to p110γ, p110α-p85α, p110β-p85β, and p110δ-p85β. Experiments were performed in duplicate with a final concentration of 50 nM of each class I PI3K complex.

D. Total Internal Reflection Fluorescence Microscopy (TIRF-M) analysis of the effect of nanobody NB7 on PI3K recruitment to supported lipid bilayers containing H-Ras(GTP) and farnesyl-Gβγ. Y647-p84/p110γ displays rapid equilibration kinetics and is insensitive to the addition of 500 nM nanobody (black arrow, 250 sec) on supported lipid bilayers containing H-Ras(GTP) and farnesyl-Gβγ.

E. Kinetics of 50 nM DY647-p84/p110γ membrane recruitment appears indistinguishable in the absence and presence of nanobody. Prior to sample injection, DY647-p84/p110γ was incubated for 10 minutes with 500 nM nanobody.

F. Representative TIRF-M images showing the localization of 50 nM DY647-p84/p110γ visualized in the absence or presence of 500 nM nanobody (+NB7). Membrane composition for panels C-E: 93% DOPC, 5% DOPS, 2% MCC-PE, Ras(GTP) covalently attached to MCC-PE, and 200 nM farnesyl-Gβγ.

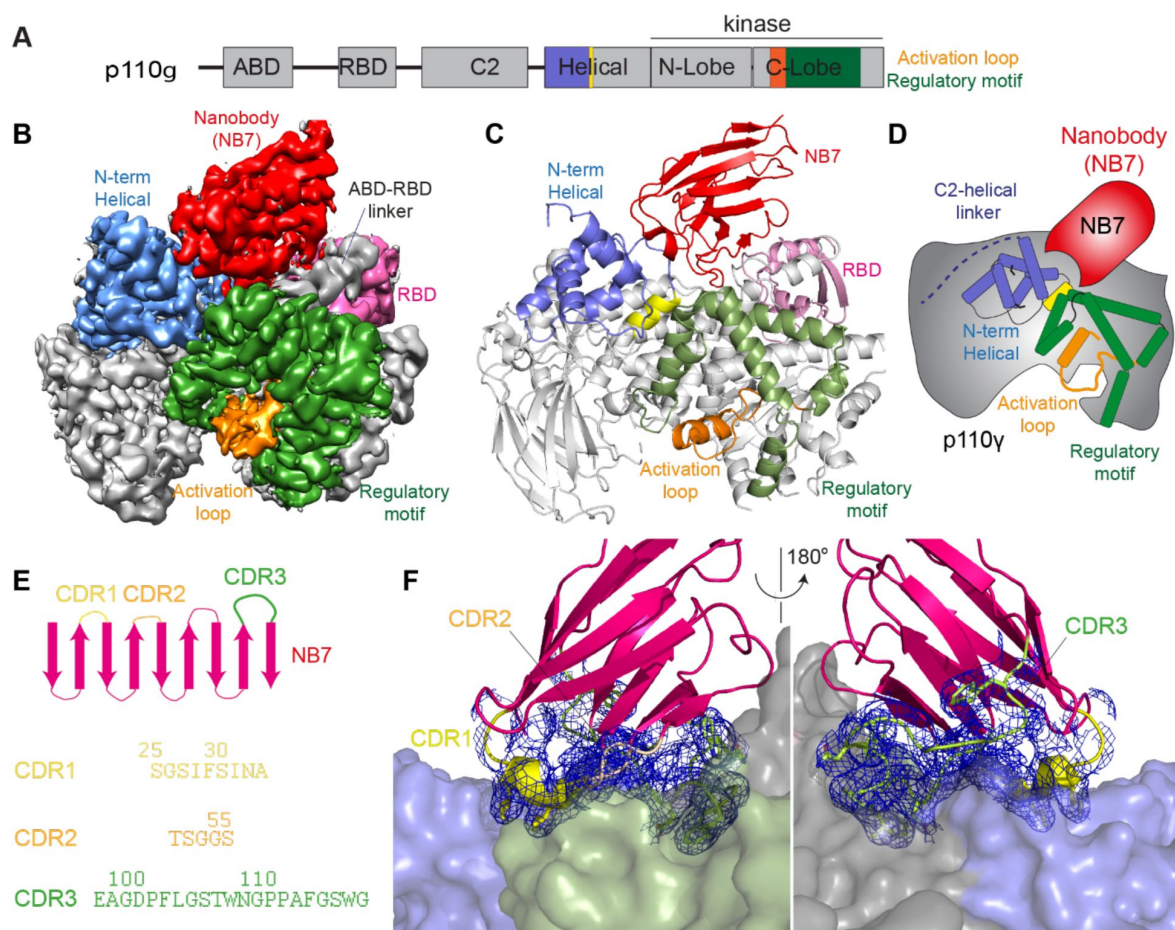


Figure 2.

Structure of p110γ bound to inhibitory nanobody NB7

- A.** Domain schematics of p110γ with helical domain (blue), activation loop (orange), and regulatory motif (green) of p110 annotated.
- B.** Density map of the p110γ-NB7 complex colored according to the schematic in **A**.
- C.** Cartoon model of the structure of p110γ bound to NB7 colored according to **A**.
- D.** Schematic depicting the key features of p110 and the nanobody binding site, colored according to panel **A**.
- E.** Domain schematic of NB7 CDR regions and their sequences.
- F.** Zoom in on the binding interface of NB7, with the CDRs colored as in panel **E**, and the electron density of the CDR regions contoured at 3σ (blue mesh).

complementarity determining region (CDR) loops of NB7 that mediate target selectivity (**Fig. 2E-F**). The interface is primarily hydrophobic, with only 8 hydrogen bonds, and 1 electrostatic interaction among the 33 interfacial residues of NB7. A pocket formed between the helical domain and the ABD-RBD linker forms the majority of the interface, with extensive interactions with the long CDR3. The CDR1 loop packed up against the N-terminal section of the helical domain, with the CDR2 loop forming the interface with the regulatory motif. Previous study of oncogenic mutants in the regulatory motif of p110 γ showed that increased dynamics mediated by these mutants increased kinase activity, putatively by breaking the autoinhibitory tryptophan lock in $\text{K}\alpha 12$ of the regulatory motif. Therefore, rigidifying the regulatory motif likely explains the molecular basis for how it prevents kinase activity. The nanobody interface is distinct from the predicted G β interface (Rathinaswamy et al., 2023) and the experimentally resolved Ras interface (Pacold et al., 2000), explaining why it can still be membrane recruited by these stimuli.

p110 γ activation by helical domain phosphorylation

To further understand the potential role helical domain dynamics in regulating p110 γ activity we searched for any possible regulatory roles of this in PI3K signalling. It has been previously identified that p110 γ is directly phosphorylated by the protein kinase PKC β on residue S582 in the helical domain (Walser et al., 2013). S582 is located on the interior of the helical domain, and would not be expected to be exposed when the N-terminal region of the helical domain is folded (**Fig. 3A**). To understand this better at a molecular level, we purified a catalytic fragment of PKC β and performed protein phosphorylation reactions on p110 γ apo, p110 γ -p84, and p110 γ -p101. We identified a phosphorylated peptide containing S582, and surprisingly, we found an additional p110 γ phosphorylation site at S594/S595 (**Fig. 3B**, Fig. S3). The S594/S595 site is also located in the N-terminal region of the helical domain, and is even more buried than S582, and would not be expected to be exposed when this region is folded (**Fig. 3A**). Dose response curves of PKC β treatment were carried out for p110 γ (**Fig. 3C**), p110 γ -p84 (**Fig. 3D**), and p110 γ -p101 (**Fig. 3E**). Both p110 γ and p110 γ -p84 showed similar dose response curves for PKC β treatment, with similar curves for S582 and S594/S595. The p110 γ -p101 complex was only very weakly phosphorylated, with <100-fold lower levels compared to p110 γ and p110 γ -p84 (**Fig. 3E**). This is consistent with the helical domain in p110 γ being more rigid when bound to p101, compared to either bound to p84 or p110 γ alone.

To provide additional insight into the molecular mechanisms underlying p110 γ phosphorylation we carried out hydrogen deuterium exchange mass spectrometry (HDX-MS) experiments on p110 γ and phosphorylated p110 γ (90.8% phosphorylated S594/595, 92% phosphorylated S582) (**Fig. 4A**). The full data underlying the experiment is available in the source data, and data processing information is in **supplemental table 2**. We have previously observed that the N-terminal region of the helical domain of apo p110 γ (residues spanning 557-630aa) shows isotope profiles that are consistent with EX1 H/D exchange kinetics (Rathinaswamy et al., 2021b, 2021c; Vadas et al., 2013; Walser et al., 2013). This is indicative of cooperative unfolding of extended protein regions, with H/D exchange occurring faster than the refolding event. This region is where the PKC phosphorylation sites are located, and may explain how the buried residues S582 and S594/S595 can be exposed to PKC. This is compatible with the observation that p110 γ -p101 is protected from phosphorylation, as it does not show EX1 kinetics in this region, whereas both p110 γ and p110 γ -p84 do (Rathinaswamy et al., 2021a).

When we compared phosphorylated p110 γ (>90.8% as measured by mass spectrometry at both sites) to unphosphorylated p110 γ we observed extensive increases in dynamics in the C2, helical domain and kinase domain (**Fig. 4A-D**). The largest increases in exchange upon phosphorylation were located in the N-terminal region of the helical domain, with the peptides directly adjacent to the phosphorylation site showing almost complete deuterium incorporation at the earliest time points of exchange. This is indicative of significant disruption of the alpha helical secondary structure in this region. When we examined the exchange profiles in this region they still underwent EX1 kinetics (**Fig. 4C**), however, phosphorylated p110 γ was enriched in the more

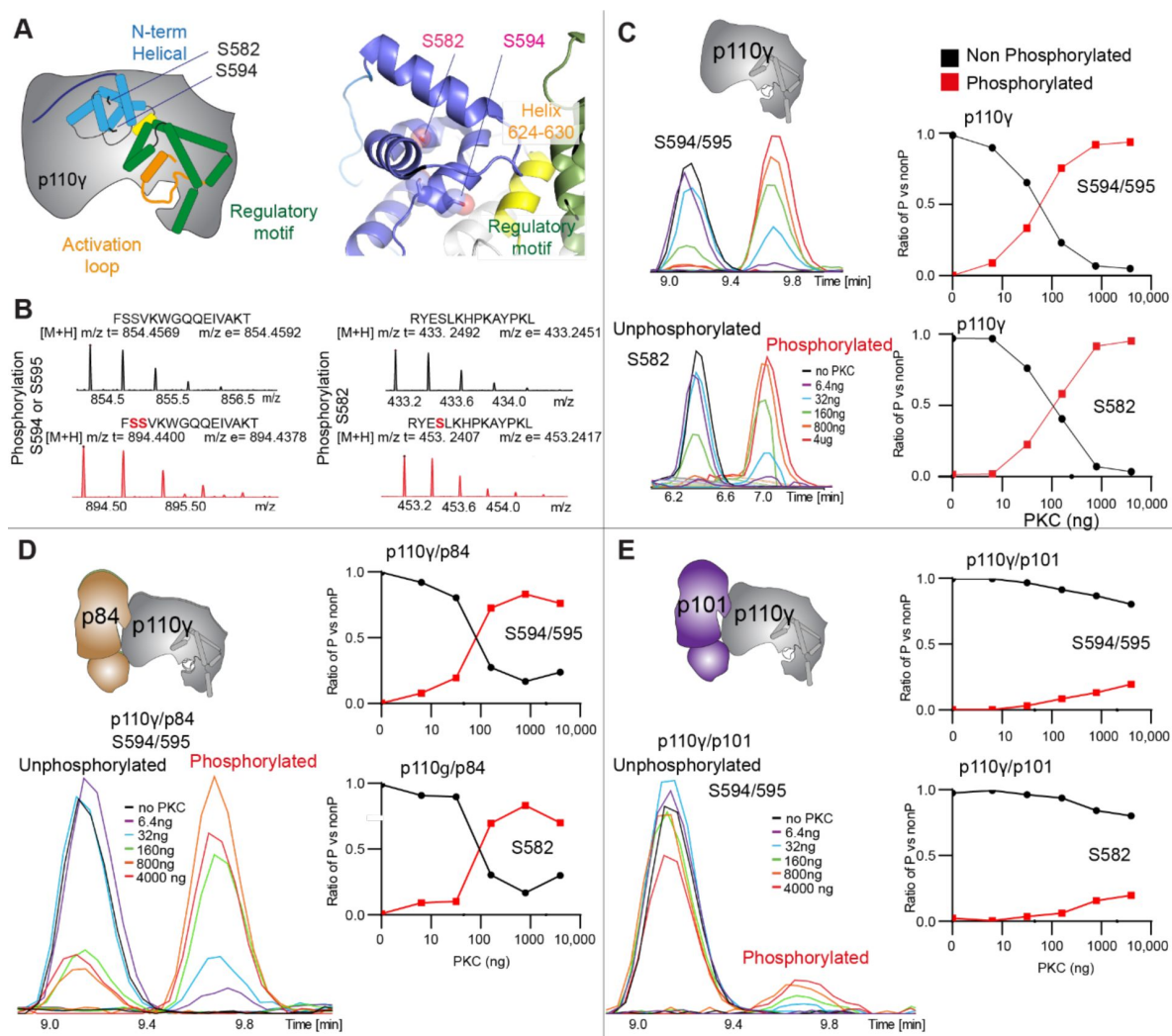


Figure 3.

PKC leads to dual phosphorylation of internal sites in the helical domain, with selectivity for apo p110 γ and p110 γ -p84 over p110 γ -p101.

A. Putative phosphorylation sites mapped on the structure of p110 γ (PDB: 7MEZ) and cartoon schematic. The regions are colored based on domain schematics featured in Fig 2A.

B. Raw MS spectra of the unphosphorylated and phosphorylated peptide for a region spanning 579-592 (RYESLKHPKAYPKL) and 593-607 (FSSVKWGQEQEIVAKT).

C-E. Extracted traces and ratios of the intensity of extracted ion traces of different phosphorylation site peptides (Top to bottom: S594/595 and S582) from © p110 γ , (D) p110 γ /p84 or (E) p110 γ /p101 samples treated with increasing concentration of PKCb according to the legend.

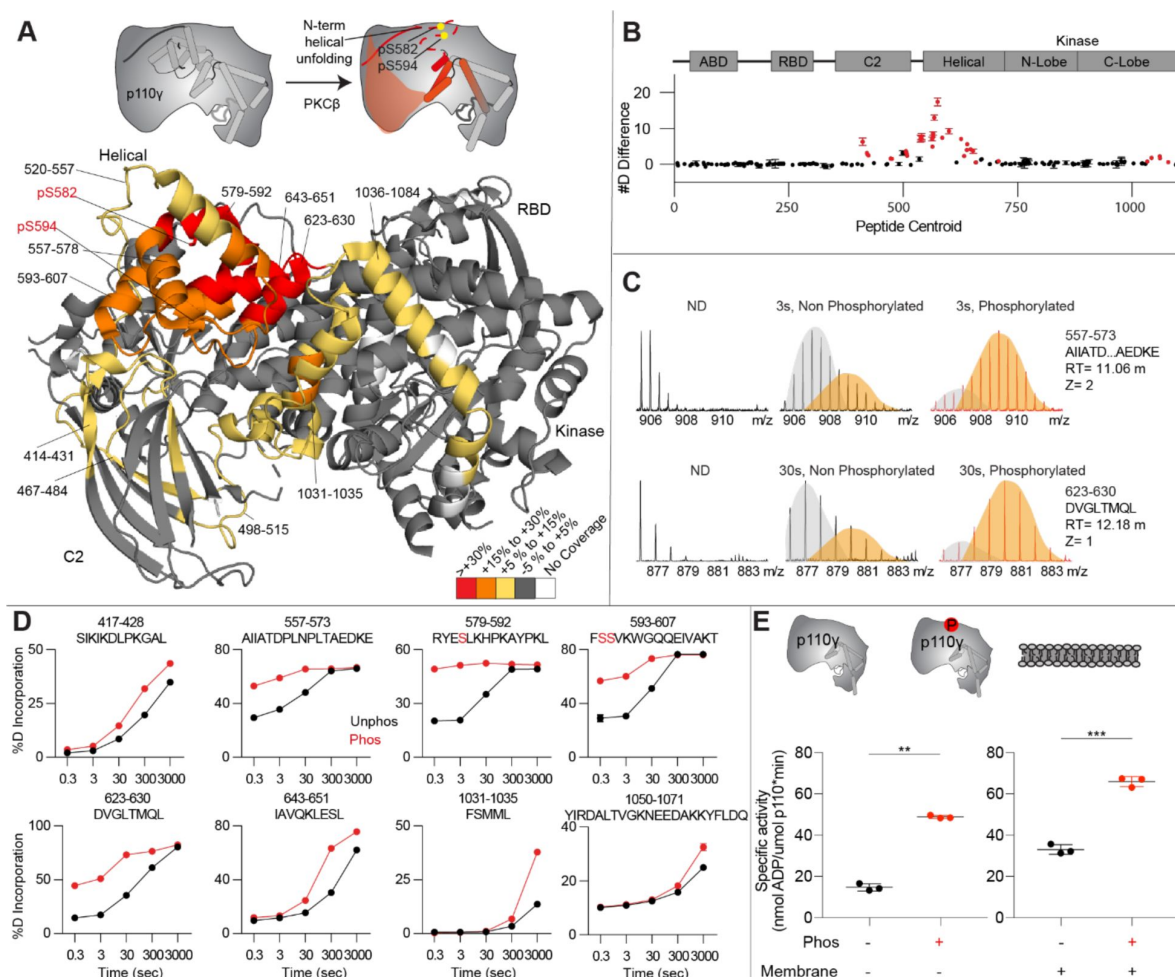


Figure 4.

Activating phosphorylation at the helical domain leads to opening of the regulatory motif

A. HDX-MS comparing apo and phosphorylated p110γ. Significant differences in deuterium exchange are mapped on to the structure and cartoon of p110γ according to the legend (PDB: 7MEZ).

B. The graph of the #D difference in deuterium incorporation for p110γ, with each point representing a single peptide. Peptides colored in red are those that had a significant change in the mutants (greater than 0.4 Da and 5% difference at any timepoint, with a two tailed t-test $p < 0.01$). Error bars are S.D. (n=3).

C. Representative bimodal distribution (EX1 kinetics) observed in the helical domain peptides of p110γ.

D. Representative p100γ peptides displaying increases in exchange in the phosphorylated state are shown. For all panels, error bars show SD (n = 3)

E. Lipid kinase activity assays of phosphorylated and non-phosphorylated p100γ (concentration, 12nM to 1000nM) ATPase activity (left) and membrane (5% phosphatidylinositol 4,5-bisphosphate (PIP2), 95% phosphatidylserine (PS)) activation (right). Significance is indicated by **(<0.001%), and ***(<0.0001%).

fully deuterated species. In addition to the regions in the helical domain, a portion of the regulatory motif of the kinase domain also showed increased deuterium exposure. This included the $\alpha 9$ - $\alpha 12$ helices that surround the activation loop of p110 γ . These increases in exchange were similar to those we had observed in a R1021C oncogenic activating mutant of *PIK3CG* (Rathinaswamy et al., 2021c).

To further explore the potential role of phosphorylation in mediating p110 γ activity, we examined the kinase activity of p110 γ for both basal ATPase and lipid membranes. Assays measured the hydrolysis of ATP to ADP, with this acting as a surrogate for PIP₃ production in the membrane assay. PKC β -mediated phosphorylation enhanced the ATPase activity of p110 γ ~2-fold in both the absence and presence of membranes (Fig. 4E).

Nanobody blocks p110 γ phosphorylation

As NB7 bound at the interface of the helical and kinase domains that is exposed upon PKC phosphorylation of p110 γ we hypothesized that the nanobody would likely alter phosphorylation. We carried out PKC phosphorylation of p110 γ , p110 γ -p101 and p110 γ bound to NB7. The presence of NB7 showed even lower phosphorylation than p110 γ -p101, with almost complete abrogation of phosphorylation at both sites (Fig. 5A-B). We also wanted to determine whether p110 γ phosphorylation reciprocally perturbed NB7 binding. BLI experiments showed that there was no detectable binding of NB7 to phosphorylated p110 γ (Fig. 5C-D), consistent with phosphorylation disrupting the N-terminal region of the p110 γ helical domain. In addition, lipid kinase assays using phosphorylated p110 γ showed no detectable difference in activity when measured in the absence and presence nanobody (Fig. 5E).

Discussion

Here we find that the helical domain is a central regulator of the p110 γ catalytic subunit of class IB PI3K, with modulation of helical dynamics through binding partners or PTMs able to either increase or decrease lipid kinase activity. These results expand on previous work defining the helical domain as a central regulator of class IA PI3Ks, where the nSH2 domain of the p85 regulatory subunits makes inhibitory interactions that significantly inhibit lipid kinase activity of all class IA catalytic subunits (p110 α , p110 β , and p110 δ) (Mandelker et al., 2009; Miled et al., 2007; Burke and Williams, 2013; Burke, 2018). This inhibitory interaction in class IA PI3Ks is disrupted in human cancers (helical hotspot mutations in *PIK3CA*) (Samuels et al., 2004) and immune disorders (helical mutations in *PIK3CD* in APDS1) (Angulo et al., 2013; Lucas et al., 2014). Class IB PI3Ks are unique compared to class IA PI3Ks, as they are not inhibited by p101 and p84 regulatory subunits, but instead potentiate GPCR activation. This lack of inhibition is due to the distinct binding interface of class IB PI3K regulatory subunits compared to class IA regulatory subunits, with only class IA regulatory subunits making direct inhibitory interactions with the kinase and helical domains of p110 catalytic subunits (Rathinaswamy et al., 2021a). Here we show that a unique surface at the interface of the helical and kinase domains of p110 γ is a potential site for the development of novel allosteric inhibitors that modulate p110 γ activity.

The previously identified inhibitory nanobody (NB7) (Rathinaswamy et al., 2021b) bound with high affinity and inhibited all complexes of p110 γ . The nanobody interface is distinct from how the nSH2 inhibits class IA PI3K activity, as its binding site is on the opposite face of the helical domain (Fig. 6A). The mechanism of inhibition is also distinct, as the nSH2-helical interaction plays a critical role in preventing membrane recruitment of inhibited class I PI3Ks, with removal of this interface either through pYXXM motif binding, or oncogenic mutations leading to increased membrane recruitment (Burke et al., 2012, 2011; Zhang et al., 2011). Analysis of the nanobody binding site compared to the structure of HRas-p110 γ or the HDX-MS supported AlphaFold-multimer prediction of G β γ -p110 γ (Rathinaswamy et al., 2023) shows that nanobody

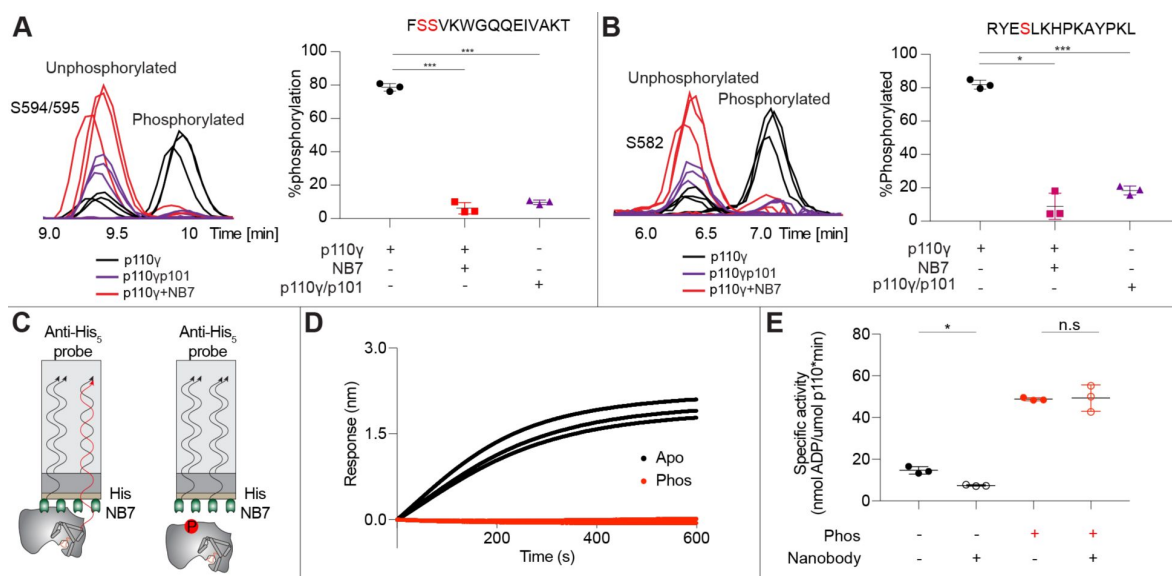


Figure 5.

Nanobody NB7 blocks PKC phosphorylation, and phosphorylation prevents nanobody binding

- A.** Graph showing the intensities of phosphorylated and non-phosphorylated p110y peptide (593-607) for PKC (500 nM) treated p110y (black), PKC treated p110y with NB7 (red) and PKC treated p110yp101 (purple). Scatter plot showing the percent phosphorylation of each complex from the left graph for the indicated peptide (n=3, right). Significance is indicated by *** (<0.0001%).
- B.** Graph showing the intensities of phosphorylated and non-phosphorylated p110y peptide (579-592) for PKC treated p110y (black), PKC treated p110y with NB7 (red) and PKC treated p110yp101 (purple). Scatter plot showing the percent phosphorylation of each complex from the left graph for the indicated peptide (n=3, right). Significance is indicated by * (<0.01%), and *** (<0.0001%).
- C.** Cartoon schematic of BLI analysis of the binding of immobilized His-NB7 to phosphorylated and non-phosphorylated p110y.
- D.** Association curves for phosphorylated and non-phosphorylated p110y (25nM) binding to His-NB7 are shown (n=3).
- E.** Kinase activity assays comparing the activation/inhibition of phosphorylated and non-phosphorylated p110y (concentration, 12nM to 1000nM) with or without nanobody (3000nM final). Significance is indicated by * (<0.05%), and NS (>0.05%).

binding does not sterically block complex formation (**Fig. 6B**). This is consistent with it not blocking membrane recruitment by Ras/Gβγ. The nanobody inhibited ATP turnover both in solution and on membranes, suggesting that it prevents formation of a catalytically competent conformation of p110γ, but still allows for membrane recruitment. Further development of small molecule allosteric binding partners in this allosteric pocket between the kinase and helical domain may reveal the specific molecular interactions in this pocket that mediate inhibition.

Oncogenic mutations are frequent in the class IA PI3Kα encoded by *PIK3CA*, with this being the 2nd most frequently mutated gene in human cancer (Lawrence et al., 2014). Mutations in p110γ encoded by *PIK3CG* in cancer are less frequent, however, they can still provide insight into regulatory mechanisms that control activity. Oncogenic mutations in the kinase domain (R1021C) and helical domain (E581K) are in close proximity to the nanobody binding site, and both would be expected to disrupt the stability of the helical domain or regulatory motif of the kinase domain (**Fig. 6C**). In addition to these mutations there are also multiple post-translational modifications that occur in this region, including inhibitory phosphorylation at T1024 (Perino et al., 2011), and activating phosphorylation at S582 (Walser et al., 2013). PKCβ is activated downstream of the IgE receptor in mast cells (Walser et al., 2013), but the full details of how this activates PI3K has been unclear. We identified an additional PKCβ phosphorylation site located in the helical domain (S594/S595) (**Fig. 6C**). Both the S582 and S594/S595 sites are not surface accessible and would require a transient opening of the helical domain for kinase accessibility. HDX-MS analysis of the helical domain of p110γ has shown that it is more dynamic than other class I PI3K isoforms (Burke and Williams, 2013; Walser et al., 2013), with the presence of the p101 regulatory subunit dramatically decreasing helical domain dynamics (Vadas et al., 2013). This putative mechanism of helical domain dynamics driving PKCβ phosphorylation is consistent with our observation that p101 subunits decreased p110γ phosphorylation >100-fold. PKCβ phosphorylation of p110γ leads to increased dynamics in both the helical and kinase domains with increased kinase activity, although only weakly compared to full activation by either membrane localised Ras or Gβγ. This increase was observed with both membrane and soluble substrate, so likely is not driven by altered membrane recruitment.

Overall, our biophysical and biochemical analysis of modulators of helical domain dynamics reveal the critical role of this domain in regulating class IB PI3K activity. This raises possibilities for development of small molecule modulators that may either increase or decrease helical domain dynamics, leading to either activation or inhibition. The high-resolution structure of an allosteric inhibitor nanobody provide initial insight into which pockets can specifically be targeted. Multiple ATP competitive p110γ selective inhibitors are in clinical trials for human cancers (Li et al., 2021), with many having significant side effects. The identification of novel inhibitory strategies provides new opportunities for targeting p110γ dysregulation in human disease.

Acknowledgements

J.E.B. is supported by the Canadian Institute of Health Research (CIHR, 168998), and the Michael Smith Foundation for Health Research (MSFHR, scholar 17686). C.K.Y. is supported by CIHR (FDN-143228, PJT-168907) and the Natural Sciences and Engineering Research Council of Canada (RGPIN-2018-03951). S.D.H. is supported by an NSF CAREER Award (MCB-2048060). This research project was supported in part by the UBC High Resolution Macromolecular Cryo-Electron Microscopy Facility (HRMEM). A portion of this research was supported by NIH grant U24GM129547 and performed at the PNCC at OHSU and accessed through EMSL (grid.436923.9), a DOE Office of Science User Facility sponsored by the Office of Biological and Environmental Research. We appreciate help from Theo Humphreys and Rose Marie Haynes with data collection at PNCC. Competing Interests: The authors declare that they have no competing interests.

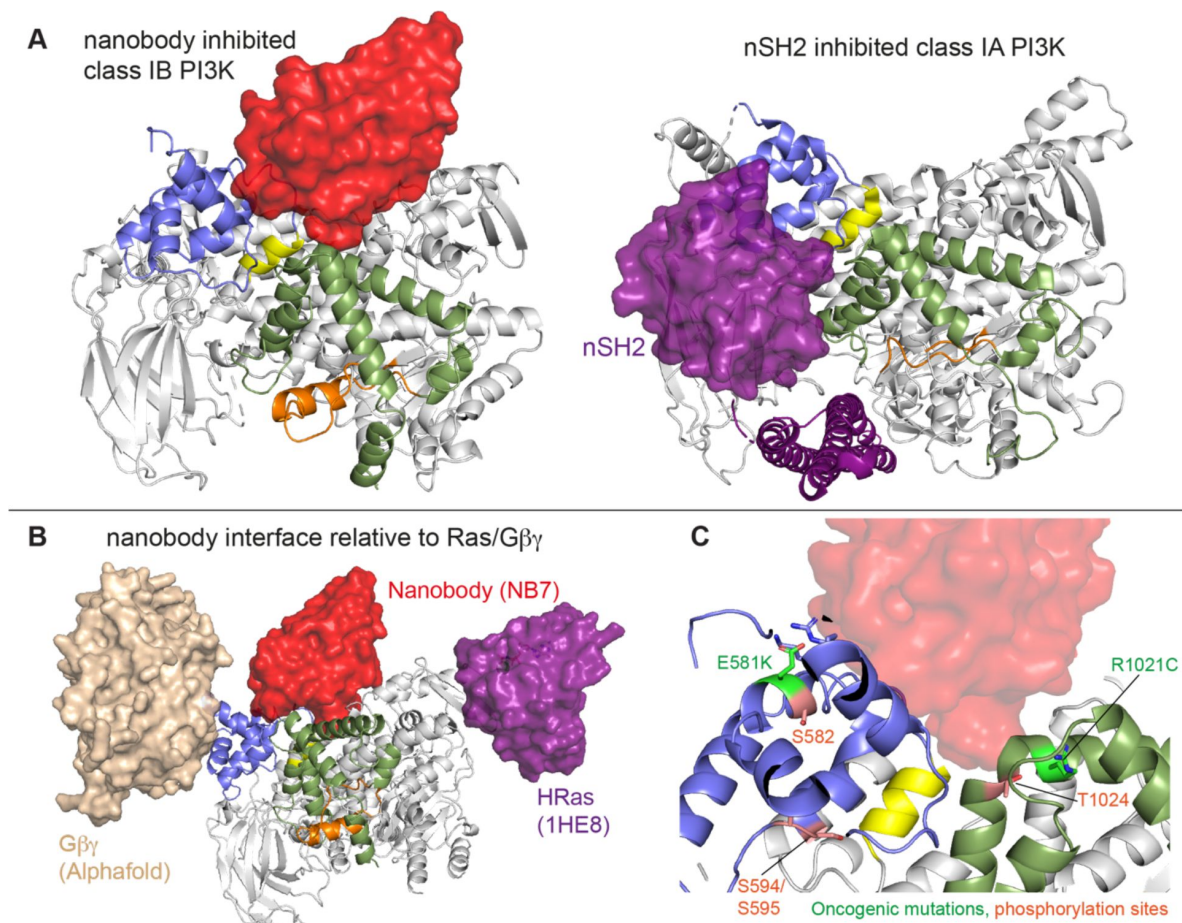


Figure 6.

Comparison of nanobody binding site compared to p85 inhibition of class IA PI3Ks and class IB activation sites

A. Comparison of the nanobody NB7 binding site in p110γ compared to the nSH2 inhibitory site in p110α (PDB: 3HHM) (Mandelker et al., 2009 [DOI](#))

B. Comparison of the nanobody NB7 binding site in p110γ compared to the X-ray structure of the Ras binding site (PDB: 1HE8) (Pacold et al., 2000 [DOI](#)) and the AlphaFold model of Gβγ bound to p110γ (Rathinaswamy et al., 2023 [DOI](#)).

C. Oncogenic mutations and post-translational modifications in spatial proximity to the nanobody binding site.

Conflict of Interest statement

JEB reports personal fees from Scorpion Therapeutics, Reactive therapeutics and Olema Oncology; and research grants from Novartis. Other authors declare no competing interests.

Methods

Resources table	SOURCE	IDENTIFIER
Bacterial and virus strains		
E.coli XL10-GOLD KanR Ultracompetent Cells	Agilent	200317
E.coli DH10EMBacY Competent Cells	Geneva Biotech	DH10EMBacY
Chemicals, peptides, and recombinant proteins		
Deuterium Oxide 99.9%	Sigma	151882
Guanosine 5'-diphosphate (GDP) sodium salt hydrate	Sigma	G7127-100MG
Guanosine 5'-triphosphate (GTP) sodium salt hydrate	Sigma	G8877-250MG
Sodium deoxycholate	Sigma	D6750

Polyoxyethylene (10) lauryl ether	Sigma	P9769
CHAPS, Molecular Biology Grade	EMD Millipore	220201
Phosphatidylserine (Porcine Brain)	Avanti	840032C
Phosphatidylethanolamine (Egg yolk)	Sigma	P6386
Cholesterol	Sigma	47127-U
Phosphatidylcholine (Egg yolk)	Avanti	840051C
Phosphatidylinositol-4,5-bisphosphate (Porcine Brain)	Avanti	840046
Sphingomyelin (Egg yolk)	Sigma	S0756
1,2-dioleoyl-sn-glycero-3-phosphocholine (DOPC)	Avanti	850375C
1,2-dioleoyl-sn-glycero-3-phospho-L-serine (18:1, DOPS)	Avanti	840035C
1,2-dioleoyl-sn-glycero-3-phosphoethanolamine-N-[4-(p-maleimidomethyl)cyclohexane-carboxamide] (18:1 MCC-PE)	Avanti	780201C
10 mg/mL beta casein solution	ThermoFisher	37528
10x PBS [pH 7.4]	Corning	46-013-CM
glucose oxidase from <i>Aspergillus niger</i> (225 U/mg)	Biophoretics	B01357.02
catalase	Sigma	C40-100MG Bovine Liver
Trolox	Cayman Chemicals	10011659
Dyomics 647 maleimide dye	Dyomics	647P1-03
Coenzyme A	Sigma	C3019
Sulfuric acid	Sigma	58105-2.5L-PC
C-Flat 2/2-T grids	FisherScientific	50-192-8327
Critical commercial assays		
Transcreeper ADP2 FI Assay (1,000 Assay, 384 Well)	BellBrook Labs	3013-1K
Deposited data		
PDB coordinate file for p110 γ -NB7 structure	PDB	8DP0
EM density file for p110 γ -NB7 complex	EMD	EMD-27627
HDX-MS and phosphorylation proteomics data	PRIDE	PXD040765
Oligonucleotides		
Fwd primer for amplifying KD of PKC β II GTATTTTCAGGGCgcccgtaccACGACCAACACTGTCT CCAAATTTG	Sigma	MR51F
Rvs primer for amplifying KD of PKC β II gactcgagcggccgcTTATAGCTCTTGACTTCGGGTTTTA AAAATTCAG	Sigma	MR51R
Fwd primer for amplifying N term of PKC β II CCATCACgcatctggcggtagtATGGCTGACCCGGCTGCG	Sigma	MR52F
Rvs primer for amplifying N term of PKC β II GCCCTGAAAATACAGGTTTTCTTTCTTCCGGGAC CTTGGTTCCC	Sigma	MR52R
Fwd primer for adding stop codon to PKC β II AGTCAAGAGCTAAgcccgcctcgagtctagagcctgc	Sigma	MR56F
Rvs primer for adding stop codon to PKC β II gactcgagcggccgcTTAGCTCTTGACTTCGGGTTTTAAA AATTCAG	Sigma	MR56R
Recombinant DNA		
pMultiBac-G β 1/G γ 2	PMID:34452907	pOP737

pACEBac1-hsp110 γ	PMID:34452907	MR30
pMultiBac-hsp110 γ -ssp101	PMID:34452907	MR22
pMultiBac-hsp110 γ -mmp84	PMID:34452907	MR24
pFastBac HRas G12V	PMID:34452907	BS9
biGBac hsp110 γ /ybbr-hsp84	PMID:36842083	HP28
biGBac hsp110 γ /ybbr-hsp101	PMID:36842083	HP29
his6-GST-PrescissionProtease-SNAP-RBD(K65E)	PMID:34452907	pSH936
his6TEV-HRas(1-184aa) C118S, C181S	PMID:34452907	pSH414
his6-G γ 2, SNAP-G β 1 (DUAL FastBac)	PMID:34452907	pSH651
pACEBAC-PKC β II (internal tev cleavage site)	This paper	pMR56
pFASTBac p110 α	PMID:28515318	pOV1181
pFASTBac p110 β	PMID:28515318	pOV1182
pFASTBac p110 δ	PMID:28515318	pOV1183
pFASTBac p85 β	This paper	EX21
Software and algorithms		
COOT-0.9.4.1	CCP4	https://www2.mrc-lmb.cam.ac.uk/personal/pemsley/coot/
Phenix-1.19.1	Open source	https://www.phenix-online.org/
PDBePISA (Proteins, Interfaces, Structures and Assemblies)	EMBL-EBI	https://www.ebi.ac.uk/pdbe/pisa/pistart.html
ESPrnt 3.0	Robert et al NAR 2014	https://esprnt.ibcp.fr
HDEaminer	Sierra Analytics	http://massspec.com/hdeaminer
GraphPad Prism 7	GraphPad	https://www.graphpad.com
PyMOL	Schroedinger	http://pymol.org
Compass Data Analysis	Bruker	https://www.bruker.com
ChimeraX	UCSF	https://www.rbvi.ucsf.edu/chimera/
ImageJ/Fiji	ImageJ	https://imagej.net/software/fiji/
Nikon NIS elements	Nikon	https://www.microscope.healthcare.nikon.com/products/software/nis-elements
cryoSPARC v.3.3.2	Structura Biotechnology	https://cryosparc.com/
Other		
Sf9 insect cells for expression	Expression Systems	94-001S
Insect cell media	Expression Systems	96-001-01
Hellmanex III cleaning solution	Fisher	14-385-864
6-well sticky-side chamber	IBIDI	80608

Plasmid Generation

Plasmids encoding Homo sapiens p110 γ (human), Mus musculus p84 (mouse), Sus scrofa p101 (porcine), and G β γ were used as previously described (Rathinaswamy et al., 2023 [DOI](#), 2021a [DOI](#)). The class IA plasmids were also used as previously described (Dornan et al., 2017 [DOI](#); Siempelkamp et al., 2017 [DOI](#)). The pDONR223-PRKCB2 (PKC β II, uniprot identifier: P05771-2) was a gift from William Hahn & David Root (Addgene plasmid #23746; <http://n2t.net/addgene> [DOI](#): 23746; RRID:Addgene_23746) (Johannessen et al., 2010 [DOI](#)). The PKC β II construct contains an internal TEV site that cleaves the catalytic domains from the C1/C2 regulatory domains (TEV site inserted between residues 320 and 321 of PRKCB, uniprot identifier: P05771-2) and it was subcloned into a pACEBAC Sf9 expression vector for protein purification. For purification, a 10 \times histidine tag, a 2 \times

strep tag, and a tobacco etch virus protease cleavage site were cloned to the N terminus of the regulatory subunits for the complex and to p110 γ and PKC β II for constructs without regulatory subunits. Full details of the plasmids are included in the resource table.

Virus Generation and Amplification

The plasmids encoding genes for insect cell expression were transformed into DH10MultiBac cells (MultiBac, Geneva Biotech) to generate baculovirus plasmid (bacmid) containing the genes of interest. Successful generation was identified by blue-white colony screening and the bacmid was purified using a standard isopropanol-ethanol extraction method. Bacteria were grown overnight (16 hours) in 3-5 mL 2xYT (BioBasic #SD7019). Cells were spun down and the pellet was resuspended in 300 μ L of 50 mM Tris-HCl, pH 8.0, 10 mM EDTA, 100 mg/mL RNase A. The pellet was lysed by the addition of 300 μ L of 1% sodium dodecyl sulfate (SDS) (W/V), 200 mM NaOH, and the reaction was neutralized by addition of 400 μ L of 3.0 M potassium acetate, pH 5.5. Following centrifugation at 21130 RCF and 4 °C (Rotor #5424 R), the supernatant was mixed with 800 μ L isopropanol to precipitate bacmid DNA. Following centrifugation, the pelleted bacmid DNA was washed with 500 μ L 70% Ethanol three times. The pellet was then air dried for 1 minute and re-suspended in 50 μ L Buffer EB (10 mM Tris-Cl, pH 8.5; All buffers from QIAprep Spin Miniprep Kit, Qiagen #27104). Purified bacmid was then transfected into Sf9 cells. 2 mL of Sf9 cells at 0.6X10⁶ cells/mL were aliquoted into a 6-well plate and allowed to attach to form a confluent layer. Transfection reactions were prepared mixing 8-12 μ g of bacmid DNA in 100 μ L 1xPBS and 12 μ g polyethyleneimine (Polyethyleneimine “Max” MW 40,000, Polysciences #24765, USA) in 100 μ L 1xPBS and the reaction was allowed to proceed for 20-30 minutes before addition to an Sf9 monolayer containing well. Transfections were allowed to proceed for 5-6 days before harvesting virus containing supernatant as a P1 viral stock.

Viral stocks were further amplified by adding P1 to Sf9 cells at $\sim 2 \times 10^6$ cells/mL (2/100 volume ratio). This amplification was allowed to proceed for 4-5 days and resulted in a P2 stage viral stock that was used in final protein expression. Harvesting of P2 viral stocks was carried out by centrifuging cell suspensions in 50 mL Falcon tubes at 2281 RCF (Beckman GS-15). To the supernatant containing virus, 5-10% inactivated fetal bovine serum (FBS; VWR Canada #97068-085) was added and the stock was stored at 4°C.

Expression and purification of PI3Ky, PI3K $\alpha/\beta/\delta$ and PKC β constructs

PI3Ky and PKC β constructs were expressed in Sf9 insect cells using the baculovirus expression system. Following 55 hours of expression, cells were harvested by centrifuging at 1680 RCF (Eppendorf Centrifuge 5810 R) and the pellets were snap-frozen in liquid nitrogen. The complex was purified through a combination of nickel affinity, streptavidin affinity and size exclusion chromatographic techniques.

Frozen insect cell pellets were resuspended in lysis buffer (20 mM Tris pH 8.0, 100 mM NaCl, 10 mM imidazole pH 8.0, 5% glycerol (v/v), 2 mM β ME), protease inhibitor (Protease Inhibitor Cocktail Set III, Sigma) and sonicated for 2 minutes (15s on, 15s off, level 4.0, Misonix sonicator 3000). Triton-X was added to the lysate to a final concentration of 0.1% and clarified by spinning at 15,000 RCF at 4°C for 45 minutes (Beckman Coulter JA-20 rotor). The supernatant was loaded onto a 5 mL HisTrap™ FF crude column (GE Healthcare) equilibrated in NiNTA A buffer (20 mM Tris pH 8.0, 100 mM NaCl, 20 mM imidazole pH 8.0, 5% (v/v) glycerol, 2 mM β ME). The column was washed with high salt NiNTA A buffer (20 mM Tris pH 8.0, 1 M NaCl, 20 mM imidazole pH 8.0, 5% (v/v) glycerol, 2 mM β ME), NiNTA A buffer, 6% NiNTA B buffer (20 mM Tris pH 8.0, 100 mM NaCl, 250 mM imidazole pH 8.0, 5% (v/v) glycerol, 2 mM β ME) and the protein was eluted with 100% NiNTA B. The eluent was loaded onto a 5 mL StrepTrap™ HP column (GE Healthcare) equilibrated in gel filtration buffer (20mM Tris pH 8.5, 100 mM NaCl, 50 mM Ammonium Sulfate and 0.5 mM TCEP). To purify PI3K $\alpha/\beta/\delta$, the purification protocol was performed as described above but instead the

protein was eluted in PI3Ka gel filtration buffer (20mM HEPES 7.5, 150mM NaCl, 0.5mM TCEP). The column was washed with the corresponding gel filtration buffer and loaded with tobacco etch virus protease. After cleavage on the column overnight, the PI3Ky protein constructs were eluted in gel filtration buffer. The protein was concentrated in a 50,000 MWCO Amicon Concentrator (Millipore) to <1 mL and injected onto a Superdex™ 200 10/300 GL Increase size-exclusion column (GE Healthcare) equilibrated in gel filtration buffer. After size exclusion, the protein was concentrated, aliquoted, frozen, and stored at -80°C. For PKCβ, the protein was eluted from the strep column in gel filtration buffer, and the eluate was then loaded on a 1ml HisTrap™ FF column to remove the his tagged LipTev. The flowthrough was collected, and the column was washed with 2ml of gel filtration buffer. These fractions were pooled and concentrated and stored at -80°C.

To purify phosphorylated p110γ, the purification protocol as described above was performed but PKCβ was added to the strep column at a molar ratio of 1:3 (PKCβII:p110) along with LipTEV, 20 mM MgCl₂ and 1mM ATP and allowed to incubate on ice for 4 hours. The protein was eluted by adding 7 ml of gel filtration buffer and treated with a second dose of PKCβ (same ratio as above) and allowed to incubate on ice for another 3 hours. For non-phosphorylated p110, same protocol was followed with the exception in the addition of PKCβ. Both the proteins were concentrated in a 50,000 MWCO Amicon Concentrator (Millipore) to <1 mL and injected onto a Superdex™ 200 10/300 GL Increase size-exclusion column (GE Healthcare) equilibrated in gel filtration buffer. The final phosphorylation level of the two sites was characterised by mass spectrometry, with these values being 92% and 90.8%, for S582 and S594/S595 respectively. After size exclusion, the protein was concentrated, aliquoted, frozen, and stored at -80°C.

Expression and Purification of lipidated Gβγ for kinase activity assays

Full length, lipidated human Gβγ (Gβ1γ2) was expressed in Sf9 insect cells and purified as described previously. After 65 hours of expression, cells were harvested, and the pellets were frozen as described above. Pellets were resuspended in lysis buffer (20 mM HEPES pH 7.7, 100 mM NaCl, 10 mM βME, protease inhibitor (Protease Inhibitor Cocktail Set III, Sigma)) and sonicated for 2 minutes (15s on, 15s off, level 4.0, Misonix sonicator 3000). The lysate was spun at 500 RCF (Eppendorf Centrifuge 5810 R) to remove intact cells and the supernatant was centrifuged again at 25,000 RCF for 1 hour (Beckman Coulter JA-20 rotor). The pellet was resuspended in lysis buffer and sodium cholate was added to a final concentration of 1% and stirred at 4°C for 1 hour. The membrane extract was clarified by spinning at 10,000 RCF for 30 minutes (Beckman Coulter JA-20 rotor). The supernatant was diluted 3 times with NiNTA A buffer (20 mM HEPES pH 7.7, 100 mM NaCl, 10 mM Imidazole, 0.1% C12E10, 10mM βME) and loaded onto a 5 mL HisTrap™ FF crude column (GE Healthcare) equilibrated in the same buffer. The column was washed with NiNTA A, 6% NiNTA B buffer (20 mM HEPES pH 7.7, 25 mM NaCl, 250 mM imidazole pH 8.0, 0.1% C12E10, 10 mM βME) and the protein was eluted with 100% NiNTA B. The eluent was loaded onto HiTrap™ Q HP anion exchange column equilibrated in Hep A buffer (20 mM Tris pH 8.0, 8 mM CHAPS, 2 mM Dithiothreitol (DTT)). A gradient was started with Hep B buffer (20 mM Tris pH 8.0, 500 mM NaCl, 8 mM CHAPS, 2 mM DTT) and the protein was eluted in ~50% Hep B buffer. The eluent was concentrated in a 30,000 MWCO Amicon Concentrator (Millipore) to < 1 mL and injected onto a Superdex™ 75 10/300 GL size exclusion column (GE Healthcare) equilibrated in Gel Filtration buffer (20 mM HEPES pH 7.7, 100 mM NaCl, 10 mM CHAPS, 2 mM TCEP). Fractions containing protein were pooled, concentrated, aliquoted, frozen and stored at -80 °C.

Expression and purification of nanobody

Nanobody NB7-PIK3CG with a C-terminal 6X His tag was expressed from a pMESy4 vector in the periplasm of WK6 *E.coli*. A 1L culture was grown to OD600 of 0.7 in Terrific Broth containing 0.1% glucose and 2mM MgCl₂ in the presence of 100 µg/mL ampicillin and was induced with 0.5 mM isopropyl-β-D-thiogalactoside (IPTG). Cells were harvested the following day by centrifuging at 2500 RCF (Eppendorf Centrifuge 5810 R) and the pellet was snap-frozen in liquid nitrogen. The

frozen pellet was resuspended in 15 mL of TES buffer containing 200 mM Tris pH 8.0, 0.5mM ethylenediaminetetraacetic acid (EDTA) and 500 mM Sucrose and was mixed for 45 minutes at 4°C. To this mixture, 30 mL of TES buffer diluted four times in water was added and mixed for 45 minutes at 4°C to induce osmotic shock. The lysate was clarified by centrifuging at 14,000 rpm for 15 minutes (Beckman Coulter JA-20 rotor). Imidazole was added to the supernatant to final concentration of 10mM loaded onto a 5 mL HisTrap™ FF crude column (GE Healthcare) equilibrated in NiNTA A buffer (20 mM Tris pH 8.0, 100 mM NaCl, 20 mM imidazole pH 8.0, 5% (v/v) glycerol, 2 mM β-mercaptoethanol (βME)). The column was washed with high salt NiNTA A buffer (20 mM Tris pH 8.0, 1 M NaCl, 20 mM imidazole pH 8.0, 5% (v/v) glycerol, 2 mM βME), followed by 100% NiNTA A buffer, then a 6% NiNTA B wash buffer (20 mM Tris pH 8.0, 100 mM NaCl, 250 mM imidazole pH 8.0, 5% (v/v) glycerol, 2 mM βME) and the protein was eluted with 100% NiNTA B. The eluent was concentrated in a 10,000 MWCO Amicon Concentrator (Millipore) to <1 mL and injected onto a Superdex™ 75 10/300 GL Increase size-exclusion column (GE Healthcare) equilibrated in gel filtration buffer (20mM Tris pH 8.5, 100 mM NaCl, 50 mM Ammonium Sulfate and 0.5 mM tris(2-carboxyethyl) phosphine (TCEP)). Following size exclusion, the protein was concentrated, frozen and stored at -80°C.

Phosphorylation analysis

For the dose–response phosphorylation of p110γ, p110/p84, and p110/p101, each protein or complex (750nM) was mixed with ATP (200 μM), GFB (20mM Tris pH 8.5, 100 mM NaCl, 50 mM Ammonium Sulfate and 0.5 mM TCEP), MgCl₂(20mM) and various amounts of PKC (4 μg, 800 ng, 160 ng, 32 ng, 6.4 ng, and 0 ng). Reactions were incubated for three hours on ice and quenched with 50 μL of ice-cold acidic quench buffer (0.7 M guanidine-HCl, 1% formic acid). followed by immediate freezing using liquid nitrogen and storage at -80 °C.

For the experiment studying the effect of nanobody on phosphorylation, p110γ or p110/p101, (500nM) was mixed with ATP (1 mM), GFB (20mM Tris pH 8.5, 100 mM NaCl, 50 mM Ammonium Sulfate and 0.5 mM TCEP), MgCl₂(20mM), with nanobody and PKC present at 1200 nM and 500nM, respectively. Reactions were incubated for one hour at room temperature and quenched with 54 μL of ice-cold acidic quench buffer (0.7 M guanidine-HCl, 1% formic acid) followed by immediate freezing using liquid nitrogen and storage at -80 °C.

Phosphorylation of all proteins was confirmed using Mass spectrometry and PEAKS7 analysis. The phosphorylated and non-phosphorylated peptide ratios were determined by generating extracted ion chromatograms for each peptide using their molecular formula and charge state in the Bruker Compass Data Analysis software. The area under each extracted curve was then extracted. The full MS quantification of each of the phosphorylated and non-phosphorylated peptide is provided in the source data.

Lipid vesicle preparation for kinase activity assays

Lipid vesicles containing 5% brain phosphatidylinositol 4,5-bisphosphate (PIP2), and 95% brain phosphatidylserine (PS), were prepared by mixing the lipids solutions in organic solvent. The solvent was evaporated in a stream of argon following which the lipid film was desiccated in a vacuum for 45 minutes. The lipids were resuspended in lipid buffer (20 mM HEPES pH 7.0, 100 mM NaCl and 10 % glycerol) and the solution was vortexed for 5 minutes followed by sonication for 15 minutes. The vesicles were then subjected to ten freeze thaw cycles and extruded 11 times through a 100-nm filter (T&T Scientific: TT-002-0010). The extruded vesicles were sub-aliquoted and stored at -80°C. Final vesicle concentration was 2 mg/mL.

Kinase Assays

All kinase assays were done using Transcreener ADP2 Fluorescence Intensity (FI) assays (Bellbrook labs) which measures ADP production. All assays used super-lipid vesicles [5% phosphatidylinositol 4,5-bisphosphate (PI(4,5)P₂), and 95% phosphatidylserine (PS)] at final concentration of 0.5 mg/mL, and ATP at a final concentration of 100 μ M.

For assays measuring the inhibition by nanobody, 4X kinase (final concentration: 330 nM for p110 γ , 300nM for p110 γ /p84 and 12nM for p110 γ /p101) was mixed with varying 4X concentrations of nanobody (final concentration: 2 μ M – 2.7nM) or kinase buffer (20mM HEPES pH 7.5, 100mM NaCl, 3mM MgCl₂, 0.03% CHAPS, 2mM TCEP, and 1mM EGTA) and allowed to sit on ice for 15 minutes. 2 μ L of protein mix was mixed with 2 μ L of lipid solution containing G β y (1 μ M final concentration), ATP (100 μ M), Super lipid (0.5mg/ml final concentration), and lipid buffer (25mM HEPES pH 7, 5% Glycerol, and 100mM NaCl) and incubated at room temperature for 60 minutes.

For assays comparing the difference in activation between phosphorylated and non-phosphorylated p110 γ , 2X kinase (final concentrations: 1 μ M – 12.3nM) was mixed with 2X lipid solutions containing ATP (100 μ M), and lipid buffer and either nanobody (3 μ M final concentration), Super lipid (0.5mg/ml final concentration) or both nanobody and lipid. The reaction was incubated at room temperature for 60 minutes.

After the 60-minute incubation, all reactions were stopped with 4 μ L of 2X stop and detect solution containing Stop and Detect buffer (20mM HEPES, 0.02% Brij-35, 400mM 40mM EDTA pH 7.5), 8 nM ADP Alexa Fluor 594 Tracer and 93.7 μ g/mL ADP2 Antibody IRDye QC-1, covered and incubated at room temperature for 1 hr before reading the fluorescence. The fluorescence intensity was measured using a SpectraMax M5 plate reader at excitation 590 nm and emission 620 nm. All data was normalized against the appropriate measurements obtained for 100 μ M ATP and 100 μ M ADP with no kinase. The percent ATP turnover was interpolated using a standard curve (0.1-100 μ M ADP). Interpolated values were then used to calculate the specific activity of the enzyme.

Biolayer interferometry

All Biolayer interferometry experiments were performed using the Octet K2 (Fortebio Inc.). When comparing nanobody binding to each complex, His-tagged nanobody was immobilized on an Anti-Penta-His biosensor for 600s, and the sensor was dipped into solutions of varying concentrations of p110 γ , p110p84, and p110p101 (50 nM – 1.9 nM) for 600s followed by a 1200s dissociation step in Octet Buffer (20 mM tris pH 8.5, 100 mM NaCl, 50 mM ammonium sulfate, 0.1% bovine serum albumin, and 0.02% Tween 20). Experiments comparing class IA PI3K versus class IB PI3K used 500 nM nanobody loaded on the Octet tip, and 50 nM of PI3Ks. When comparing nanobody binding to phosphorylated and unphosphorylated p110 γ , His-tagged nanobody was immobilized on an Anti-Penta-His biosensor for 600 s, and the sensor was dipped into solutions of either phosphorylated or non-phosphorylated p110 γ at a final concentration of 25 nM for 600s followed by a dissociation step for 600s. The average K_D (dissociation constant) was calculated from the binding curves based on their global fit to a 1:1 binding model.

Supported lipid bilayer TIRF microscopy experiments

The membrane binding dynamics of Dy647-p84-p110 γ were measured in the absence and presence of nanobody 7 (NB7) using TIRF microscopy. As previously described (Rathinaswamy et al., 2023 [\[4\]](#)), supported lipid bilayers were formed using 50 nm extruded small unilamellar vesicles (SUVs) containing the following lipids: 1,2-dioleoyl-sn-glycero-3-phosphocholine (18:1 DOPC, Avanti # 850375C), 1,2-dioleoyl-sn-glycero-3-phospho-L-serine (18:1 DOPS, Avanti # 840035C), 1,2-dioleoyl-sn-glycero-3-phosphoethanolamine-N-[4-(p-maleimidomethyl)cyclohexane-carboxamide] (18:1 MCC-PE, Avanti # 780201C). Lipid compositions reported in figure legends represent the molar percentage of each lipid species.

To create SLBs, a total concentration of 0.25 mM lipids was solvated in 1x PBS [pH 7.4] and deposited on Piranha etched glass coverslips (25 x 75 mm) adhered to an IBIDI chamber. After a 30-minute incubation, membranes were washed with 4 mL of 1x PBS [pH 7.4] and then blocked for 10 minutes with 1 mg/mL beta casein (Thermo FisherSci, Cat# 37528) in 1x PBS [pH 7.4] (Corning, Cat# 46-013-CM). To conjugate H-Ras to maleimide lipids (MCC-PE), blocked membranes were incubated with 30 μ M H-Ras(GDP) in buffer containing 1x PBS [pH 7.4], 1 mM $MgCl_2$, 50 μ M GDP, and 0.1 mM TCEP for 2 hours. The membrane conjugation reaction was terminated after 2 hours with 1x PBS [pH 7.4] containing 5 mM β -mercaptoethanol (β ME). Membranes were then washed and stored in 1x PBS [pH 7.4] until performing the TIRF-M membrane binding experiments. H-Ras was purified as previously described (Rathinaswamy et al., 2023 [DOI](#)).

To perform the TIRF-M membrane binding assays, 200 nM farnesyl-G β y was equilibrated into the supported membranes for 30 minutes. In parallel, nucleotide exchange of H-Ras(GDP) was performed by adding 50 nM guanine nucleotide exchange factor (SosCat) in 1x PBS [pH 7.4], 1 mM $MgCl_2$, 50 μ M GDP. To measure membrane binding, Dy647-p84-p110y was diluted into the following buffer: 20 mM HEPES [pH 7.0], 150 mM NaCl, 50 μ M GTP, 1 mM ATP, 5 mM $MgCl_2$, 0.5 mM EGTA, 20 mM glucose, 200 μ g/mL beta casein (ThermoScientific, Cat# 37528), 20 mM BME, 320 μ g/mL glucose oxidase (Serva, #22780.01 *Aspergillus niger*), 50 μ g/mL catalase (Sigma, #C40-100MG Bovine Liver), and 2 mM Trolox. Trolox was prepared as previously described (Hansen et al., 2019 [DOI](#)). Perishable reagents (i.e. glucose oxidase, catalase, and Trolox) were added 10 minutes before image acquisition.

TIRF-M experiments were performed using an inverted Nikon Ti2 microscope with a 100x Nikon (1.49 NA) oil immersion objective. The x-axis and y-axis positions were controlled using a Nikon motorized stage. Dy647-p84-p110y was excited with a 637 nm diode laser (OBIS laser diode, Coherent Inc. Santa Clara, CA) controlled with an acousto-optic tunable filter (AOTF) and laser launch built by Vortran (Sacramento, CA). The power output measured through the objective for single particle imaging was 1-3 mW. Excitation light passing through quad multi-pass dichroic filter cube (Semrock). Fluorescence emission passed through Nikon emission filter wheel containing the following 25 mm ET700/75M emission filters (Semrock) before being detected on iXion Life 897 EMCCD camera (Andor Technology Ltd., UK). All TIRF-M experiments were performed at room temperature (23°C). Microscope hardware was controlled using Nikon NIS elements. Data analysis was performed using ImageJ/Fiji and Prism graphing program.

Cryo-EM Sample Preparation and Data Collection

3 μ L of purified nanobody-bound p110y at 0.45 mg/ml was adsorbed onto C-Flat 2/2-T grids that were glow discharged for 25 s at 15 mA. Grids were then plunged into liquid ethane using a Vitrobot Mark IV (Thermo Fisher Scientific) with the following settings: -5 blot force, 1.5 s blot time, 100% humidity and 4 °C. Vitrified specimens were screened for ice and particle quality at the UBC High resolution macromolecular electron microscopy (HRMEM) facility using a 200-kV Glacios transmission electron microscope equipped with a Falcon 3EC direct electron detector (DED). Clipped grids were sent to the Pacific Northwest Cryo-EM Center (PNCC) where 7,322 movies were collected using a Titan Krios equipped with a Gatan K3 DED and a BioQuantum K3 energy filter with a slit width of 20 eV. The movies were collected at a physical pixel size of 0.830 Å/pix and a total dose of 50e⁻/Å² over 50 frames.

Cryo-EM image analysis

The data were processed using cryoSPARC v3.3.2 (Punjani et al., 2017 [DOI](#)). The movies were pre-processed by patch motion correction using default settings except Fourier-cropping by a factor of 2, followed by patch CTF estimation using default settings. A 3D map of PI3K p110y-p101 complex (EMD-23808) was used to create 2D projections for use as templates to auto-pick 1,463,553 particles. Particles were extracted with a box size of 380 pixels, Fourier cropped to a box size of 96 pixels and subjected to 2D classification. After discarding classes with obvious noise and no

features, 795,162 particles were used for multiple rounds of *ab initio* reconstruction and heterogeneous refinement using 4 or 5 classes. 365,178 particles, which generated the two best 3D reconstruction, were used to carry out Per-particle local-motion correction with 760 pixels box size later downsized to 380 pixels followed by several rounds of *ab initio* reconstruction and heterogeneous refinement using 3 or 5 classes. 149,603 from best class were further refined by homogeneous refinement and a final Non-Uniform (NU)-refinement which generated a reconstruction with an overall resolution of 3.02 Å based on the Fourier shell correlation (FSC) 0.143 criterion.

Building the structural model of p110γ-NB7

The previous structural model of full length p110γ from the complex of p110γ-p101(PDB: 7MEZ) (Rathinaswamy et al., 2021a [↗](#)) was fit into the map using Chimera (Pettersen et al., 2004 [↗](#)). A model of the nanobody was generated using AlphaFold2 using the Colabfold v1.5.2 server (Mirdita et al., 2022 [↗](#)). The CDR loops were removed from this initial model, and the remaining nanobody was fit into the map using Chimera. The final structure was built by iterative rounds of automated model building in Phenix, manual model building in COOT (Emsley et al., 2010 [↗](#)), and refinement in Phenix.real_space_refine using realspace, rigid body, and adp refinement with tight secondary structure restraints (Afonine et al., 2012 [↗](#)). This allowed for unambiguous building of the CDRs of the nanobody, and their interface with p110γ. The full refinement and validation statistics are shown in **Supplemental table 1** [↗](#).

Hydrogen Deuterium eXchange Mass Spectrometry

Exchange reactions to assess differences in p110γ upon phosphorylation were carried out at 20°C in 10 μL volumes with final concentrations of 1.6 μM for both apo and phosphorylated p110γ. A total of two conditions were assessed: p110γ apo and PKCβ phosphorylated p110γ. The hydrogen-deuterium exchange reaction was initiated by the addition of 8 μL D₂O buffer (94.3% D₂O, 100 mM NaCl, 20 mM HEPES pH 7.5) to the 2 μL protein for a final D₂O concentration of 75.4%. Exchange was carried out over five time points (3s on ice, and 3s, 30s, 300s and 3000s at 20°C) and the reaction was quenched with addition of 60 μL of ice-cold acidic quench buffer (0.7 M guanidine-HCl, 1% formic acid). After quenching, samples were immediately frozen in liquid nitrogen and stored at -80°C. All reactions were carried out in triplicate.

Protein Digestion and MS/MS Data Collection

Protein samples were rapidly thawed and injected onto an integrated fluidics system containing a HDx-3 PAL liquid handling robot and climate-controlled chromatography system (LEAP Technologies), a Dionex Ultimate 3000 UHPLC system, as well as an Impact HD QTOF Mass spectrometer (Bruker). The protein was run over two immobilized pepsin columns (Applied Biosystems; Poroszyme™ Immobilized Pepsin Cartridge, 2.1 mm x 30 mm; Thermo-Fisher 2-3131-00; at 10°C and 2°C respectively) at 200 μL/min for 3 minutes. The resulting peptides were collected and desalted on a C18 trap column [Acquity UPLC BEH C18 1.7 mm column (2.1 x 5 mm); Waters 186003975]. The trap was subsequently eluted in line with an ACQUITY 1.7 μm particle, 100 x 1 mm² C18 UPLC column (Waters 186002352), using a gradient of 3-35% B (buffer A, 0.1% formic acid; buffer B, 100% acetonitrile) over 11 min immediately followed by a gradient of 35-80% B over 5 minutes. MS experiments acquired over a mass range from 150 to 2200 mass/charge ratio (m/z) using an electrospray ionization source operated at a temperature of 200°C and a spray voltage of 4.5 kV.

Peptide Identification

Peptides were identified using data-dependent acquisition following tandem MS/MS experiments (0.5 s precursor scan from 150-2000 m/z; twelve 0.25 s fragment scans from 150-2000 m/z). MS/MS datasets were analyzed using PEAKS7 (PEAKS), and a false discovery rate was set at 0.1% using a

database of purified proteins and known contaminants. Same approach was used to identify phosphorylated and non-phosphorylated peptides for our in-vitro phosphorylation experiments, with variable phosphorylation of STY residues was added to the search. The search parameters were set with a precursor tolerance of 20 parts per million, fragment mass error 0.02 Da, and charge states from 1 to 8, with a selection criterion of peptides that had a $-10\log P$ score of >24.03 for phosphorylated and >23.05 for non-phosphorylated. The MS/MS spectra of the PKC phosphorylated peptides are included in Fig S3.

Mass Analysis of Peptide Centroids and Measurement of Deuterium Incorporation

HD-Examiner Software (Sierra Analytics) was used to automatically calculate the level of deuterium incorporation into each peptide. All peptides were manually inspected for correct charge state, correct retention time, and appropriate selection of isotopic distribution. Deuteration levels were calculated using the centroid of the experimental isotope clusters. HDX-MS results are presented with no correction for back exchange shown in the Source data, with the only correction being applied correcting for the deuterium oxide percentage of the buffer used in the exchange (75.4%). Changes in any peptide at any time point greater than specified cut-offs (5% and 0.45 Da) and with an unpaired, two-tailed t-test value of $p < 0.01$ was considered significant. A number of peptides in the helical domain showed isotope distributions consistent with EX1 H/D exchange. Attempts to define the relative percentages of each population using HDExaminer were extremely noisy, so representative EX1 profiles are shown in **Fig. 3C** [↗](#). The raw peptide deuterium incorporation graphs for a selection of peptides with significant differences are shown in **Fig. 4D** [↗](#), with the raw data for all analysed peptides in the source data. To allow for visualization of differences across all peptides, we utilized number of deuterium difference (#D) plots (**Fig. 4B** [↗](#)). These plots show the total difference in deuterium incorporation over the entire H/D exchange time course, with each point indicating a single peptide. The data analysis statistics for all HDX-MS experiments are in **Supplemental Table 2** [↗](#) according to the guidelines of (Masson et al., 2019 [↗](#)). The mass spectrometry proteomics data have been deposited to the ProteomeXchange Consortium via the PRIDE partner repository (Perez-Riverol et al., 2022 [↗](#)) with the dataset identifier PXD040765.

Supplemental information for

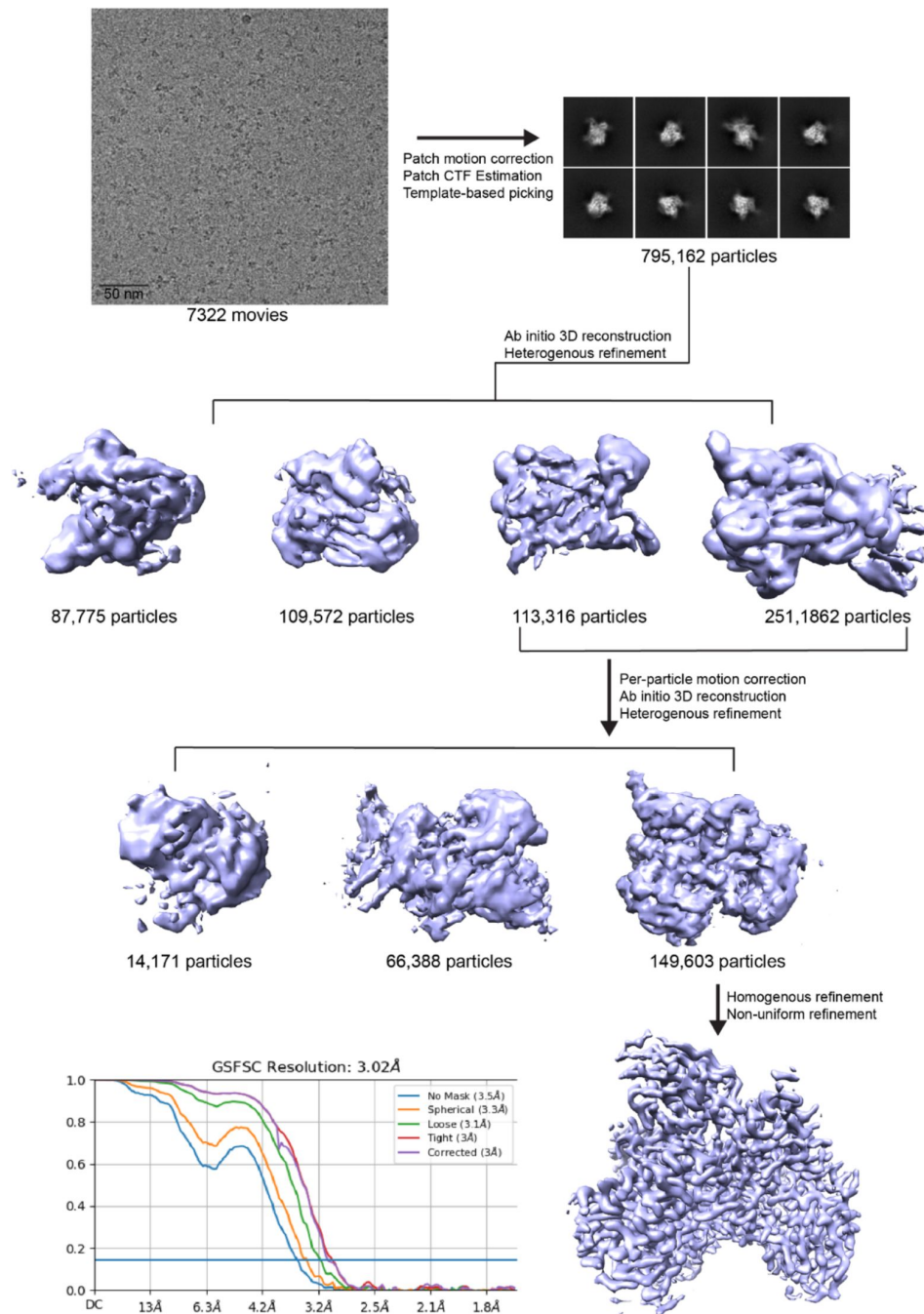


Figure S1.

p110 γ -NB7 complex cryo-EM analysis workflow (related to main figure 2 [↗](#)):

cryo-EM processing workflow of p110 γ -NB7 complex are shown in order of a representative micrographs, representative 2D classification and 3D reconstruction processing strategy. Bottom left shows Gold-standard Fourier shell Correlation (FSC) curve of final round on non-uniform homogenous refinement.

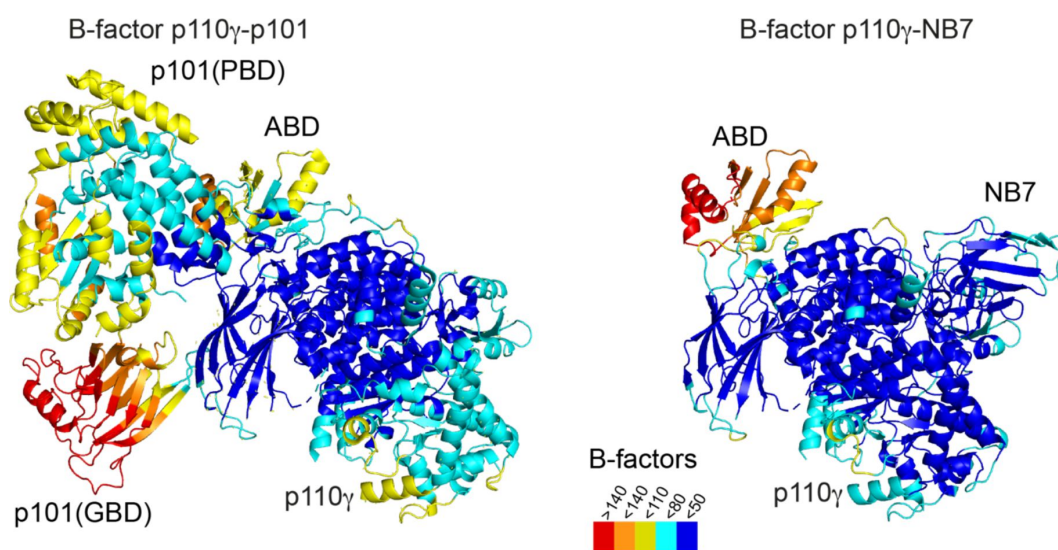


Figure S2.

Comparison of full length p110 γ bound to NB7 compared to p110 γ -p101 (related to main figure 2 [↗](#)):

The structure of the p110 γ -p101 complex (PDB:7MEZ) compared to the NB7-p110 γ complex is shown colored according to B factor based on the legend.

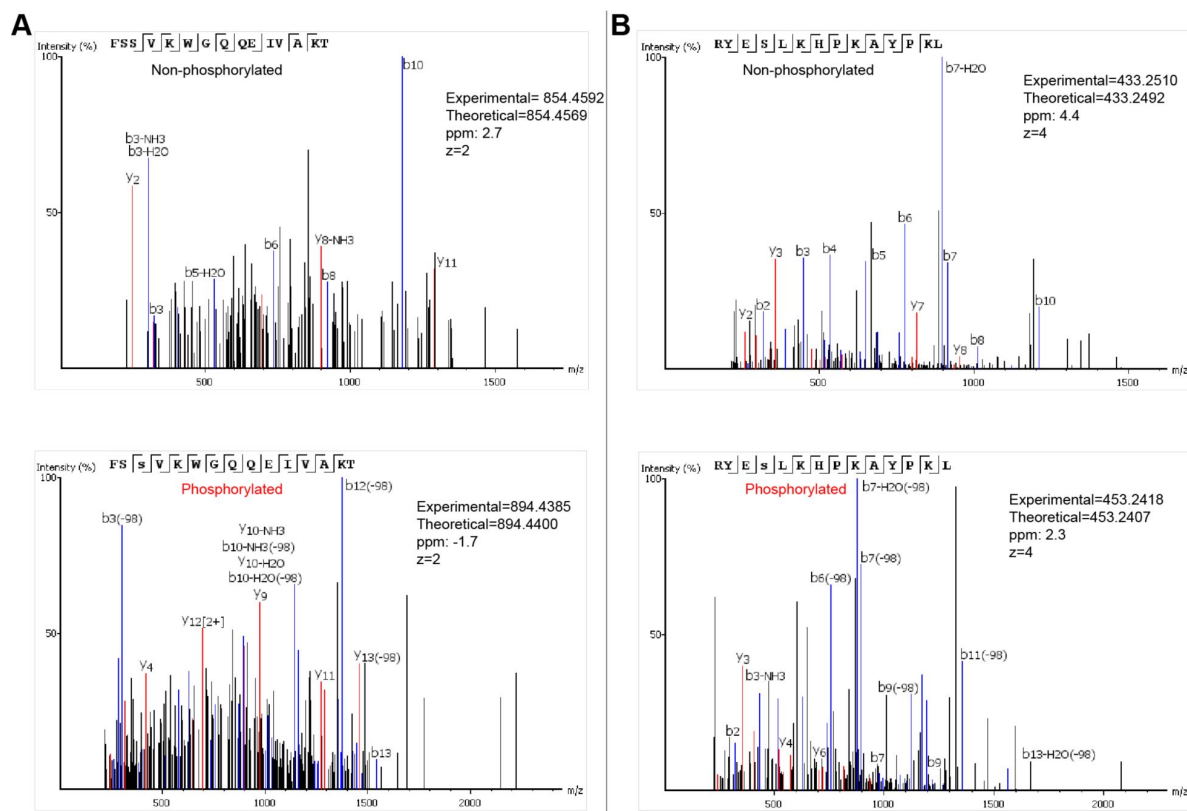


Figure S3

(related to main figure 3 [↗](#))

MS/MS spectra of peptides spanning S582 and S594/S595 for both phosphorylated and unphosphorylated states. The theoretical and experimental mass are annotated for all peptides.

	p110 γ -NB7 EMD- 27627 PDB: 8DP0
Data collection and processing	
Magnification	
Voltage (kV)	300
Electron exposure (e/ Å ²)	50
Defocus range (nM)	500-2500
Pixel size (Å)	
Symmetry imposed	C1
Initial particle images (no.)	795,162
Final particle images (no.)	149,603
Map resolution (Å)	3.02
FSC threshold	0.143
Map resolution range (Å)	2.6-4.4
Refinement	
Initial model used (PDB)	7MEZ (p110 γ only)
Model Resolution (Å)	3.02
FSC threshold	0.5
Map sharpening B factor	Sharpened locally
Model composition	
Non-hydrogen atoms	8737
Protein residues	1,066
Ligands	0
B-factors	
Protein	52.4
Validation	
Mol probability score	1.29
Clashscore	5.33
Poor rotamers (%)	0.0
Ramachandran	
Favored	98.41
Allowed	1.59
Outliers	0.0
R.m.s. deviations	
Bond lengths (Å)	0.002
Bond angles (°)	0.490
Model to map fit (CC_mask)	0.86

Supplementary table 1.

Cryo-EM data collection, refinement and validation statistics (related to main figure 2 [↗](#))

Data set	p110γ unphosphorylated	p110γ phosphorylated
HDX reaction details	%D ₂ O=75.5% pH _(read) =7.5 Temp=4°C, 20°C	%D ₂ O=75.5% pH _(read) =7.5 Temp=4°C, 20°C
HDX time course (seconds)	3s at 4°C, 3s, 30s, 300s, 3000s at 20 °C	3s at 4°C, 3s, 30s, 300s, 3000s at 20 °C
HDX controls	N/A	N/A
Back-exchange	No correction, deuterium levels are relative	No correction, deuterium levels are relative
Number of peptides	244	244
Sequence coverage	98.4%	98.4%
Average peptide /redundancy	Length= 15.2 Redundancy= 3.3	Length= 15.2 Redundancy= 3.3
Replicates	3	3
Repeatability	Average StDev=0.53%	Average StDev=0.57%
Significant differences in HDX	>5% and >0.4 Da and unpaired t-test ≤0.01	>5% and >0.4 Da and unpaired t-test ≤0.01

Supplementary table 2.

HDX-MS data collection and validation statistics (related to main figure 4 [↗](#))

References

- Afonine PV, Grosse-Kunstleve RW, Echols N, Headd JJ, Moriarty NW, Mustyakimov M, Terwilliger TC, Urzhumtsev A, Zwart PH, Adams PD (2012) **Towards automated crystallographic structure refinement with phenix.refine** *Acta Crystallogr D Biol Crystallogr* **68**:352–367 <https://doi.org/10.1107/S0907444912001308>
- Angulo I *et al.* (2013) **Phosphoinositide 3-kinase δ gene mutation predisposes to respiratory infection and airway damage** *Science* **342**:866–871 <https://doi.org/10.1126/science.1243292>
- Becattini B *et al.* (2011) **PI3Kgamma within a nonhematopoietic cell type negatively regulates diet-induced thermogenesis and promotes obesity and insulin resistance** *Proc Natl Acad Sci USA* **108**:E854–63 <https://doi.org/10.1073/pnas.1106698108/-/DCSupplemental>
- Bell K, Sunose M, Ellard K, Cansfield A, Taylor J, Miller W, Ramsden N, Bergamini G, Neubauer G (2012) **SAR studies around a series of triazolopyridines as potent and selective PI3Ky inhibitors** *Bioorg Med Chem Lett* **22**:5257–5263 <https://doi.org/10.1016/j.bmcl.2012.06.049>
- Bohnacker T, Marone R, Collmann E, Calvez R, Hirsch E, Wymann M (2009) **PI3Kgamma adaptor subunits define coupling to degranulation and cell motility by distinct PtdIns(3,4,5)P3 pools in mast cells** *Sci Signal* **2** <https://doi.org/10.1126/scisignal.2000259>
- Bohnacker T *et al.* (2017) **Deconvolution of Buparlisib's mechanism of action defines specific PI3K and tubulin inhibitors for therapeutic intervention** *Nat Commun* **8** <https://doi.org/10.1038/ncomms14683>
- Breasson L *et al.* (2017) **PI3Ky activity in leukocytes promotes adipose tissue inflammation and early-onset insulin resistance during obesity** *Sci Signal* **10** <https://doi.org/10.1126/scisignal.aaf2969>
- Burke JE (2018) **Structural Basis for Regulation of Phosphoinositide Kinases and Their Involvement in Human Disease** *Mol Cell* **71**:653–673 <https://doi.org/10.1016/j.molcel.2018.08.005>
- Burke JE, Perisic O, Masson GR, Vadas O, Williams RL (2012) **Oncogenic mutations mimic and enhance dynamic events in the natural activation of phosphoinositide 3-kinase p110 α (PIK3CA)** *Proc Natl Acad Sci USA* **109**:15259–15264 <https://doi.org/10.1073/pnas.1205508109>
- Burke JE, Vadas O, Berndt A, Finegan T, Perisic O, Williams RL (2011) **Dynamics of the phosphoinositide 3-kinase p110 δ interaction with p85 α and membranes reveals aspects of regulation distinct from p110 α** *Structure* **19**:1127–1137 <https://doi.org/10.1016/j.str.2011.06.003>
- Burke JE, Williams RL (2015) **Synergy in activating class I PI3Ks** *Trends in Biochemical Sciences* **40**:88–100 <https://doi.org/10.1016/j.tibs.2014.12.003>
- Burke JE, Williams RL (2013) **Dynamic steps in receptor tyrosine kinase mediated activation of class IA phosphoinositide 3-kinases (PI3K) captured by H/D exchange (HDX-MS)** *Adv Biol Regul* **53**:97–110 <https://doi.org/10.1016/j.jbior.2012.09.005>

- Campa CC *et al.* (2018) **Inhalation of the prodrug PI3K inhibitor CL27c improves lung function in asthma and fibrosis** *Nat Commun* **9**:5232–16 <https://doi.org/10.1038/s41467-018-07698-6>
- Camps M *et al.* (2005) **Blockade of PI3Kγ suppresses joint inflammation and damage in mouse models of rheumatoid arthritis** *Nat Med* **11**:936–943 <https://doi.org/10.1038/nm1284>
- De Henau O *et al.* (2016) **Overcoming resistance to checkpoint blockade therapy by targeting PI3Kγ in myeloid cells** *Nature* **539**:443–447 <https://doi.org/10.1038/nature20554>
- Deladeriere A, Gambardella L, Pan D, Anderson KE, Hawkins PT, Stephens LR (2015) **The regulatory subunits of PI3Kγ control distinct neutrophil responses** *Sci Signal* **8** <https://doi.org/10.1126/scisignal.2005564>
- Dornan GL, Siempelkamp BD, Jenkins ML, Vadas O, Lucas CL, Burke JE (2017) **Conformational disruption of PI3Kδ regulation by immunodeficiency mutations in PIK3CD and PIK3R1** *Proc Natl Acad Sci USA* **114**:1982–1987 <https://doi.org/10.1073/pnas.1617244114>
- Emsley P, Lohkamp B, Scott WG, Cowtan K (2010) **Features and development of Coot** *Acta Crystallogr D Biol Crystallogr* **66**:486–501 <https://doi.org/10.1107/S0907444910007493>
- Evans CA *et al.* (2016) **Discovery of a Selective Phosphoinositide-3-Kinase (PI3K)-γ Inhibitor (IPI-549) as an Immuno-Oncology Clinical Candidate** *ACS Med Chem Lett* **7**:862–867 <https://doi.org/10.1021/acsmedchemlett.6b00238>
- Gangadhara G *et al.* (2019) **A class of highly selective inhibitors bind to an active state of PI3Kγ** *Nature Chemical Biology* **15**:348–357 <https://doi.org/10.1038/s41589-018-0215-0>
- Hansen SD, Huang WYC, Lee YK, Bieling P, Christensen SM, Groves JT. (2019) **Stochastic geometry sensing and polarization in a lipid kinase-phosphatase competitive reaction** *Proc Natl Acad Sci U S A* **116**:15013–15022 <https://doi.org/10.1073/pnas.1901744116>
- Hawkins PT, Stephens LR. (2015) **PI3K signalling in inflammation** *Biochim Biophys Acta* **1851**:882–897 <https://doi.org/10.1016/j.bbailip.2014.12.006>
- Jenkins ML, Ranga-Prasad H, Parson MAH, Harris NJ, Rathinaswamy MK, Burke JE (2023) **Oncogenic mutations of PIK3CA lead to increased membrane recruitment driven by reorientation of the ABD, p85 and C-terminus** *Nat Commun* **14** <https://doi.org/10.1038/s41467-023-35789-6>
- Jin JR, Gogvadze E, Xavier AR, Bohnacker T, Voelzmann J, Wymann MP (2020) **PI3Kγ Regulatory Protein p84 Determines Mast Cell Sensitivity to Ras Inhibition-Moving Towards Cell Specific PI3K Targeting?** *Front Immunol* **11** <https://doi.org/10.3389/fimmu.2020.585070>
- Johannessen CM *et al.* (2010) **COT drives resistance to RAF inhibition through MAP kinase pathway reactivation** *Nature* **468**:968–972 <https://doi.org/10.1038/nature09627>
- Kaneda MM *et al.* (2016) **Macrophage PI3Kγ Drives Pancreatic Ductal Adenocarcinoma Progression** *Cancer Discov* **6**:870–885 <https://doi.org/10.1158/2159-8290.CD-15-1346>
- Kaneda MM *et al.* (2016) **PI3Kγ is a molecular switch that controls immune suppression** *Nature* **539**:437–442 <https://doi.org/10.1038/nature19834>

- Kurig B *et al.* (2009) **Ras is an indispensable coregulator of the class IB phosphoinositide 3-kinase p87/p110gamma** *Proc Natl Acad Sci USA* **106**:20312–20317 <https://doi.org/10.1073/pnas.0905506106>
- Laffargue M, Calvez R, Finan P, Trifilieff A, Barbier M, Altruda F, Hirsch E, Wymann MP (2002) **Phosphoinositide 3-kinase gamma is an essential amplifier of mast cell function** *Immunity* **16**:441–451
- Lanahan SM, Wymann MP, Lucas CL (2022) **The role of PI3Ky in the immune system: new insights and translational implications** *Nat Rev Immunol* <https://doi.org/10.1038/s41577-022-00701-8>
- Lawrence MS, Stojanov P, Mermel CH, Robinson JT, Garraway LA, Golub TR, Meyerson M, Gabriel SB, Lander ES, Getz G (2014) **Discovery and saturation analysis of cancer genes across 21 tumour types** *Nature* **505**:495–501 <https://doi.org/10.1038/nature12912>
- Li H, Prever L, Hirsch E, Gulluni F (2021) **Targeting PI3K/AKT/mTOR Signaling Pathway in Breast Cancer** *Cancers (Basel)* **13** <https://doi.org/10.3390/cancers13143517>
- Li Z, Jiang H, Xie W, Zhang Z, Smrcka AV, Wu D (2000) **Roles of PLC-beta2 and -beta3 and PI3Kgamma in chemoattractant-mediated signal transduction** *Science* **287**:1046–1049 <https://doi.org/10.1126/science.287.5455.1046>
- Liu X, Zhou Q, Hart JR, Xu Y, Yang S, Yang D, Vogt PK, Wang M-W (2022) **Cryo-EM structures of cancer-specific helical and kinase domain mutations of PI3Kα** *Proc Natl Acad Sci U S A* **119** <https://doi.org/10.1073/pnas.2215621119>
- Lucas CL *et al.* (2014) **Dominant-activating germline mutations in the gene encoding the PI(3)K catalytic subunit p110δ result in T cell senescence and human immunodeficiency** *Nat Immunol* **15**:88–97 <https://doi.org/10.1038/ni.2771>
- Luo L, Wall AA, Tong SJ, Hung Y, Xiao Z, Tarique AA, Sly PD, Fantino E, Marzolo M-P, Stow JL (2018) **TLR Crosstalk Activates LRP1 to Recruit Rab8a and PI3Ky for Suppression of Inflammatory Responses** *Cell Rep* **24**:3033–3044 <https://doi.org/10.1016/j.celrep.2018.08.028>
- Mandelker D, Gabelli SB, Schmidt-Kittler O, Zhu J, Cheong I, Huang C-H, Kinzler KW, Vogelstein B, Amzel LM (2009) **A frequent kinase domain mutation that changes the interaction between PI3Kalpha and the membrane** *Proc Natl Acad Sci USA* **106**:16996–17001 <https://doi.org/10.1073/pnas.0908444106>
- Masson GR *et al.* (2019) **Recommendations for performing, interpreting and reporting hydrogen deuterium exchange mass spectrometry (HDX-MS) experiments** *Nat Methods* **16**:595–602 <https://doi.org/10.1038/s41592-019-0459-y>
- Miled N, Yan Y, Hon W-C, Perisic O, Zvelebil M, Inbar Y, Schneidman-Duhovny D, Wolfson HJ, Backer JM, Williams RL (2007) **Mechanism of two classes of cancer mutations in the phosphoinositide 3-kinase catalytic subunit** *Science* **317**:239–242 <https://doi.org/10.1126/science.1135394>
- Mirdita M, Schütze K, Moriwaki Y, Heo L, Ovchinnikov S, Steinegger M (2022) **ColabFold: making protein folding accessible to all** *Nat Methods* **19**:679–682 <https://doi.org/10.1038/s41592-022-01488-1>

- Okkenhaug K (2013) **Signaling by the phosphoinositide 3-kinase family in immune cells** *Annu Rev Immunol* **31**:675–704 <https://doi.org/10.1146/annurev-immunol-032712-095946>
- Pacold ME, Suire S, Perisic O, Lara-Gonzalez S, Davis CT, Walker EH, Hawkins PT, Stephens L, Eccleston JF, Williams RL. (2000) **Crystal structure and functional analysis of Ras binding to its effector phosphoinositide 3-kinase gamma** *Cell* **103**:931–943
- Perez-Riverol Y *et al.* (2022) **The PRIDE database resources in 2022: a hub for mass spectrometry-based proteomics evidences** *Nucleic Acids Res* **50**:D543–D552 <https://doi.org/10.1093/nar/gkab1038>
- Perino A *et al.* (2011) **Integrating Cardiac PIP(3) and cAMP Signaling through a PKA Anchoring Function of p110gamma** *Mol Cell* **42**:84–95 <https://doi.org/10.1016/j.molcel.2011.01.030>
- Pettersen EF, Goddard TD, Huang CC, Couch GS, Greenblatt DM, Meng EC, Ferrin TE (2004) **UCSF Chimera--a visualization system for exploratory research and analysis** *J Comput Chem* **25**:1605–1612 <https://doi.org/10.1002/jcc.20084>
- Punjani A, Rubinstein JL, Fleet DJ, Brubaker MA (2017) **cryoSPARC: algorithms for rapid unsupervised cryo-EM structure determination** *Nat Methods* **14**:290–296 <https://doi.org/10.1038/nmeth.4169>
- Rathinaswamy MK, Burke JE (2019) **Class I phosphoinositide 3-kinase (PI3K) regulatory subunits and their roles in signaling and disease** *Adv Biol Regul* **100**:657 <https://doi.org/10.1016/j.jbior.2019.100657>
- Rathinaswamy MK *et al.* (2021) **Structure of the phosphoinositide 3-kinase (PI3K) p110γ-p101 complex reveals molecular mechanism of GPCR activation** *Sci Adv* **7** <https://doi.org/10.1126/sciadv.abj4282>
- Rathinaswamy MK, Fleming KD, Dalwadi U, Pardon E, Harris NJ, Yip CK, Steyaert J, Burke JE (2021) **HDX-MS-optimized approach to characterize nanobodies as tools for biochemical and structural studies of class IB phosphoinositide 3-kinases** *Structure* **29**:1371–1381 <https://doi.org/10.1016/j.str.2021.07.002>
- Rathinaswamy MK, Gaieb Z, Fleming KD, Borsari C, Harris NJ, Moeller BE, Wyman MP, Amaro RE, Burke JE (2021) **Disease-related mutations in PI3Kγ disrupt regulatory C-terminal dynamics and reveal a path to selective inhibitors** *Elife* **10** <https://doi.org/10.7554/eLife.64691>
- Rathinaswamy MK *et al.* (2023) **Molecular basis for differential activation of p101 and p84 complexes of PI3Kγ by Ras and GPCRs** *Cell Rep* **42** <https://doi.org/10.1016/j.celrep.2023.112172>
- Rynkiewicz NK *et al.* (2020) **Gβγ is a direct regulator of endogenous p101/p110γ and p84/p110γ PI3Kγ complexes in mouse neutrophils** *Sci Signal* **13** <https://doi.org/10.1126/scisignal.aaz4003>
- Samuels Y *et al.* (2004) **High frequency of mutations of the PIK3CA gene in human cancers** *Science* **304** <https://doi.org/10.1126/science.1096502>

Shymanets A, Prajwal P, Bucher K, Beer-Hammer S, Harteneck C, Nürnberg B (2013) **p87 and p101 subunits are distinct regulators determining class IB PI3K specificity** *J Biol Chem* **288**:31059–68 <https://doi.org/10.1074/jbc.M113.508234>

Siempelkamp BD, Rathinaswamy MK, Jenkins ML, Burke JE (2017) **Molecular mechanism of activation of class IA phosphoinositide 3-kinases (PI3Ks) by membrane-localized HRas** *J Biol Chem* **292**:12256–12266 <https://doi.org/10.1074/jbc.M117.789263>

Stephens LR *et al.* (1997) **The Gbg sensitivity of a PI3K is dependent upon a tightly associated adaptor, p101** *Cell* **89**:105–114

Takeda AJ *et al.* (2019) **Human PI3Ky deficiency and its microbiota-dependent mouse model reveal immunodeficiency and tissue immunopathology** *Nat Commun* **10**:4364–12 <https://doi.org/10.1038/s41467-019-12311-5>

Vadas O *et al.* (2013) **Molecular determinants of PI3Ky-mediated activation downstream of G-protein-coupled receptors (GPCRs)** *Proc Natl Acad Sci U S A* **110**:18862–18867 <https://doi.org/10.1073/pnas.1304801110>

Vanhaesebroeck B, Perry MWD, Brown JR, André F, Okkenhaug K (2021) **PI3K inhibitors are finally coming of age** *Nat Rev Drug Discov* **20**:741–769 <https://doi.org/10.1038/s41573-021-00209-1>

Vasan N, Cantley LC (2022) **At a crossroads: how to translate the roles of PI3K in oncogenic and metabolic signalling into improvements in cancer therapy** *Nat Rev Clin Oncol* <https://doi.org/10.1038/s41571-022-00633-1>

Walker EH, Perisic O, Ried C, Stephens L, Williams RL (1999) **Structural insights into phosphoinositide 3-kinase catalysis and signalling** *Nature* **402**:313–320 <https://doi.org/10.1038/46319>

Walser R *et al.* (2013) **PKCβ phosphorylates PI3Ky to activate it and release it from GPCR control** *PLoS Biol* **11** <https://doi.org/10.1371/journal.pbio.1001587>

Zhang X, Vadas O, Perisic O, Anderson KE, Clark J, Hawkins PT, Stephens LR, Williams RL (2011) **Structure of lipid kinase p110β/p85β elucidates an unusual SH2-domain-mediated inhibitory mechanism** *Mol Cell* **41**:567–578 <https://doi.org/10.1016/j.molcel.2011.01.026>

Article and author information

Noah J Harris

Department of Biochemistry and Microbiology, University of Victoria, Victoria, British Columbia, V8W 2Y2, Canada

Meredith L Jenkins

Department of Biochemistry and Microbiology, University of Victoria, Victoria, British Columbia, V8W 2Y2, Canada
ORCID iD: [0000-0002-0685-5048](https://orcid.org/0000-0002-0685-5048)

Sung-Eun Nam

Department of Biochemistry and Molecular Biology, The University of British Columbia, Vancouver, British Columbia V6T 1Z3, Canada

Manoj K Rathinaswamy

Department of Biochemistry and Microbiology, University of Victoria, Victoria, British Columbia, V8W 2Y2, Canada

Matthew AH Parson

Department of Biochemistry and Microbiology, University of Victoria, Victoria, British Columbia, V8W 2Y2, Canada

ORCID iD: [0000-0001-6270-559X](https://orcid.org/0000-0001-6270-559X)

Harish Ranga-Prasad

Department of Biochemistry and Microbiology, University of Victoria, Victoria, British Columbia, V8W 2Y2, Canada

Udit Dalwadi

Department of Biochemistry and Molecular Biology, The University of British Columbia, Vancouver, British Columbia V6T 1Z3, Canada

Brandon E Moeller

Department of Biochemistry and Microbiology, University of Victoria, Victoria, British Columbia, V8W 2Y2, Canada

Eleanor Sheekey

Department of Biochemistry and Microbiology, University of Victoria, Victoria, British Columbia, V8W 2Y2, Canada

Scott D Hansen

Department of Chemistry and Biochemistry, Institute of Molecular Biology, University of Oregon, Eugene, OR 97403

ORCID iD: [0000-0001-7005-6200](https://orcid.org/0000-0001-7005-6200)

Calvin K Yip

Department of Biochemistry and Molecular Biology, The University of British Columbia, Vancouver, British Columbia V6T 1Z3, Canada

For correspondence: calvin.yip@ubc.ca

ORCID iD: [0000-0003-1779-9501](https://orcid.org/0000-0003-1779-9501)

John E Burke

Department of Biochemistry and Microbiology, University of Victoria, Victoria, British Columbia, V8W 2Y2, Canada, Department of Biochemistry and Molecular Biology, The University of British Columbia, Vancouver, British Columbia V6T 1Z3, Canada

For correspondence: jeburke@uvic.ca

ORCID iD: [0000-0001-7904-9859](https://orcid.org/0000-0001-7904-9859)

Copyright

© 2023, Harris et al.

This article is distributed under the terms of the [Creative Commons Attribution License](https://creativecommons.org/licenses/by/4.0/), which permits unrestricted use and redistribution provided that the original author and source are credited.

Editors

Reviewing Editor

Amy Andreotti

Iowa State University, Ames, United States of America

Senior Editor

Volker Dötsch

Goethe University, Frankfurt am Main, Germany

Reviewer #1 (Public Review):

The authors examine signaling factors that differentiate parallel routes to activating phosphoinositide 3-kinase gamma (PI3K γ). Dissecting the convergent pathways that control PI3K γ activity is critical because PI3K γ is a therapeutic target for treating inflammatory disease and cancer. Here, the authors employ a multipronged approach to reveal new aspects for how p84 and p101 pair with p110 γ to activate the PI3K γ heterodimer. The key instigator to this study is a previously reported inhibitory Nanobody, NB7. The hypothesized mechanism for NB7 allosteric inhibition of p84- p110 γ was previously proposed to involve blockage of the Ras-binding domain. The authors revise the allosteric inhibition model based on meticulous profiling of various PI3K γ complex interactions with NB7. In parallel, a cryo-EM-derived model of NB7 bound to the p110 γ subunit convincingly reveals a Nanobody interaction pocket involving the helical domain and regulatory motifs of the kinase domain. This revelation shifts the focus to the helical domain, a known target of PKC phosphorylation. While the connections between NB7 interactions and the effects of PKC phosphorylation are sometimes tenuous, it could be argued that the Nanobody served as a tool to reveal the importance of the helical domain to p110 γ regulation.

The sites of PKC-mediated p110 γ helical domain phosphorylation were unexpectedly inaccessible in the available structural models. Nevertheless, mass spectrometry (MS)-based phosphorylation profiling indicates that PKC can phosphorylate the helical domain of p110 γ and p84/p110 γ (but not p101/p110 γ) in vitro. The authors hypothesize that helical domain dynamics dictate susceptibility to PKC phosphorylation. To explore this notion, carefully executed, rigorous H/D exchange MS (HDX-MS) experiments were performed comparing phosphorylated vs. unphosphorylated p110 γ . Notably, this design reveals more about the consequences of p110 γ phosphorylation, rather than the mechanisms of p84/p101 promoting/resisting phosphorylation. Nevertheless, HDX-MS is very well suited to exploring secondary structure dynamics, and helical domain phosphorylation strikingly increases dynamics consistent with increased regional accessibility. The increased dynamics also nicely map to the pocket enveloped by the inhibitory NB7 Nanobody.

Ultimately, this study reveals an unexpected p110 γ pocket that allows an engineered Nanobody to allosterically inhibit PI3K γ complexes. The cryo-EM characterization of the interaction inspired an HDX-MS investigation of known sites of phosphorylation in the region. These insights could be linked to differences/convergences of p84 and p101 complex formation and activation of PI3K γ , and future work may clarify these mechanisms further. The data presented herein will also be useful for broadening the target surface for future therapeutic developments. New allosteric connections between effector binding sites and post-translational modifications are always welcome.

- <https://doi.org/10.7554/eLife.88058.1.sa1>

Reviewer #2 (Public Review):

Harris et al. have described the cryo-EM structure of PI3K p110gamma in a complex with a nanobody that inhibits the enzyme. This provided the first structure of full-length of PI3Kgamma in the absence of a regulatory subunit. This nanobody is a potent allosteric inhibitor of the enzyme, and might provide a starting point for developing allosteric, isotype-specific inhibitors of the enzyme. One distinct effect of the nanobody is to greatly decrease the dynamics of the enzyme as shown by HDX-MS, which is consistent with a growing body of observations suggesting that for the whole PI3K superfamily, enzyme activators increase enzyme dynamics.

The most remarkable outcome of the study is that upon observing the site of nanobody binding, the authors searched the literature and found that there was a previous report of a PKCbeta phosphorylation of PI3Kgamma in the helical domain that is near the nanobody binding site. This led the authors to re-examine the consequence of the phosphorylation armed with better structural models and the tools to study the effects of this phosphorylation on enzyme dynamics. They found that the site of phosphorylation is buried in the helical domain, suggesting that a large conformational change would have to take place to enable the phosphorylation. HDX-MS showed that phosphorylation at three sites clustered in the helical domain generate a distinctly different conformation with rapid deuterium exchange. This suggests that the phosphorylation locks the enzyme in a more dynamic state. Their enzyme kinetics show that the phosphorylated, dynamic enzyme is activated.

While this phosphorylation was reported before, the authors have provided a mechanism for why this activates the enzyme, and they have shown why binders that stabilise the helical domain (such as binding to the p101 regulatory subunit and the nanobody) prevent the phosphorylation. It is this insight into the dynamics of the PI3Kgamma that will likely be the long-lasting influence of the work.

The paper is well written and the methods are clear.

- <https://doi.org/10.7554/eLife.88058.1.sa0>